A Climatology of Drylines in the Interior of Subtropical Southern Africa

L. VAN SCHALKWYK,[a] R. C. BLAMEY,[a] L. L. DYSON,[b] AND C. J. C. REASON[a]

[a] *Department of Oceanography, University of Cape Town, Cape Town, South Africa*
[b] *Department of Geography, Geoinformatics and Meteorology, University of Pretoria, Pretoria, South Africa*

(Manuscript received 28 December 2021, in final form 19 July 2022)

ABSTRACT: A climatology of synoptic drylines on the subtropical southern African interior plateau (SAP) is developed using ERA5 reanalysis specific humidity and surface temperature gradients and an objective detection algorithm. Drylines are found to occur regularly during spring and summer (September–March), and almost daily during December of that period, but rarely in winter. A westward shift in peak dryline frequency takes place through the summer. Drylines peak first over the eastern parts of the SAP during November with a mean of 10 drylines and then over the central (mean of 12) and western SAP (mean of 20) in December. During midsummer, drylines over the eastern SAP are negatively correlated with drylines in the west. Between 1980 and 2020, a significant correlation exists between ENSO and dryline days over the eastern ($r = 0.44$; p value = 0.004) and central ($r = 0.41$; p value = 0.008) SAP with fewer drylines (up to 10) occurring during years with increased surface moisture and more drylines (up to 45) occurring during years with decreased surface moisture. Drylines forming over the eastern parts of the SAP were more likely to move westward than drylines over the central and western parts. Onset times across the SAP show that drylines have a tendency to form during either the late morning to early afternoon (1100 and 1400 LST) or during the early evening hours (1700 and 2000 LST), suggesting that the surface heat trough (Kalahari heat low) and westward moisture transport mechanisms, such as the Limpopo low-level jet and ridging highs, are responsible for the formation of most drylines across the SAP.

SIGNIFICANCE STATEMENT: "Drylines" are used to describe boundaries separating regions of very dry air from those with much higher moisture content. The importance of these drylines is that they tend to act as a trigger for thunderstorms, which can produce severe weather. In this study, we build a long-term climatological description of drylines in subtropical southern Africa. We find that drylines are most frequent over eastern South Africa during the early summer, a time when storms with large hail and damaging winds are most likely to occur. Drylines are sensitive to moisture circulation patterns and respond differently during El Niño and La Niña years, with generally more drylines during El Niño over eastern South Africa and fewer during La Niña.

KEYWORDS: Atmosphere; Africa; Southern Hemisphere; Subtropics; Climatology; ENSO; Mesoscale systems; Drylines; Convective storms; Surface observations

1. Introduction

When dry subsided air and moist maritime or tropical air masses meet, the result is a quasi-linear airmass boundary or front that separates dry air from moist air and manifests as a strong moisture gradient on a surface dewpoint analysis. A similar boundary can also form between tropical and subtropical/midlatitude air masses. The importance of these moisture fronts or drylines is that their formation has often been linked with the development of convective storms, through acting as zones of enhanced convergence, which in turn can produce severe weather (Rhea 1966; Weston 1972; Duell and Van Den Broeke 2016). Drylines have been documented on all continental areas falling within the tropics or midlatitudes, including the United States (Schaefer 1986; Hoch and Markowski 2005; Schultz et al. 2007), India (Akter and Tsuboki 2017), Germany (Spänkuch et al. 2011), northeastern China (Qin and Chen 2017), northern Australia (Arnup and Reeder 2007), Argentina (Bechis et al. 2020), and southern Africa (Taljaard 1958; Howard and Washington 2019). In each of these regions, drylines contain different characteristics and the formation mechanisms that result in their development are linked to the regional synoptic circulation and local orography.

In the United States, drylines over the Great Plains frequently occur during spring and early summer when moist air streaming northward from the Gulf of Mexico comes in contact with dry air that originates over the high-lying plains of Mexico and the western mountain ranges of the United States (Schaefer 1986). The Andes mountains in western Argentina/Chile reach over 6000 m in places, and the interaction of this high topography with the midlatitude westerlies contributes to the formation of drylines on the low-lying central Argentinian plains farther to the east (Bechis et al. 2020). Adiabatic warming of prefrontal westerlies, as they descend on the lee side of the southern Andes range of mountains, leads to a dryline over the plains as this warm dry air mass encounters moist, tropical northerlies, often enhanced by the South American low-level jet from the Amazon River basin farther north (Marengo et al. 2004). During spring and early summer, intense surface heating inland results in a sea-breeze circulation along the northern coastline of Australia while also causing the development of an elongated heat trough extending across the northern interior equatorward of ~20°S. The sea breeze advects tropical maritime air inland where it encounters dry continental air and

Corresponding author: Lynette van Schalkwyk, lynvanschalkwyk@gmail.com

DOI: 10.1175/JCLI-D-21-1005.1

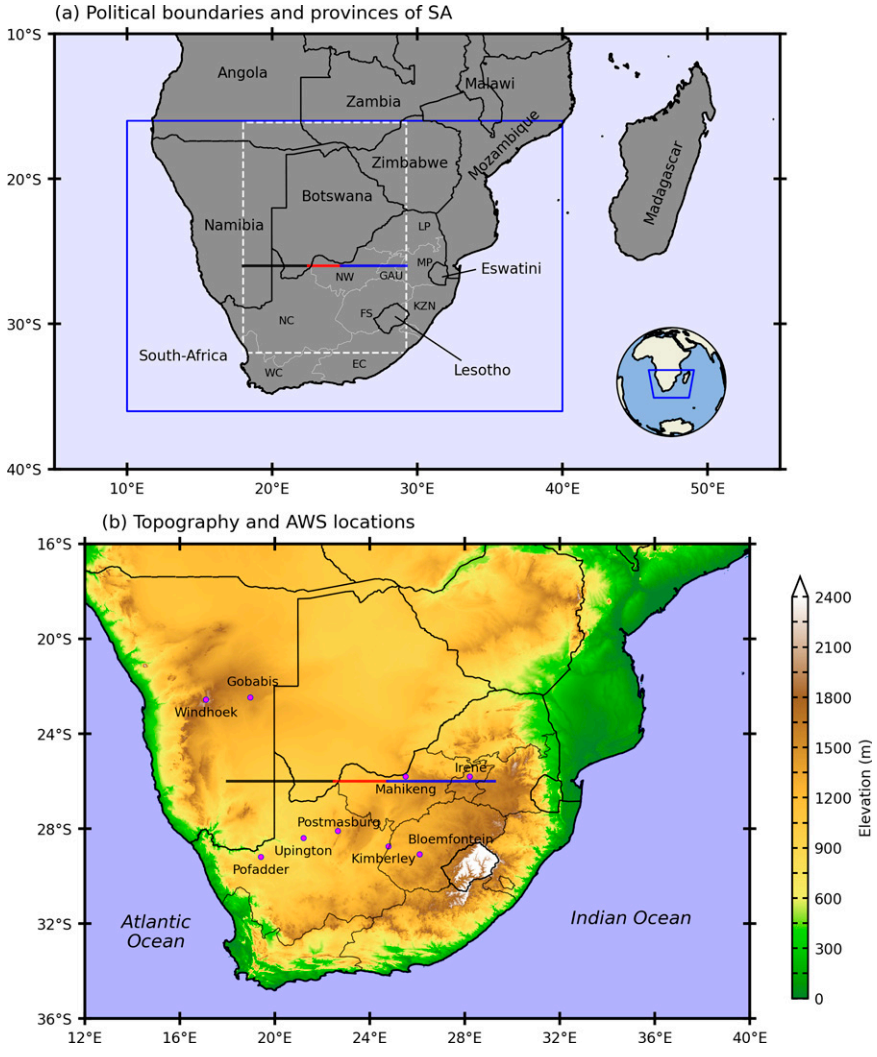

FIG. 1. (a) Political boundaries of southern Africa with provincial boundaries and abbreviations for South Africa. The study region is indicated by a solid blue-outlined rectangle, and the southern African plateau (SAP) is outlined in dashed white. The horizontal line indicates segments of analysis along 26°S, with black, red, and blue representing SAP-West, SAP-Transition, and SAP-East, respectively. (b) Regional topography (shaded; m) and names/locations of AWS used.

forms a diffuse moisture gradient during the afternoon. At night this moisture gradient intensifies as a result of the acceleration of air parcels from both air masses toward the low, forming a dryline (Arnup and Reeder 2007).

In southern Africa, two distinct drylines have been documented in the literature. In the tropics, the "Congo air boundary" (CAB) stretches from the Angolan coast to eastern Zambia (see Fig. 1a for country locations) during austral spring and early summer before the main rainy season starts (Howard and Washington 2019). This east–west-oriented dryline separates moist low-level westerlies originating from the tropical southeast Atlantic from a dry, easterly flow across much of tropical southern Africa. The second dryline has a northwest–southeast orientation and extends from northern Namibia across Botswana and into central South Africa (Taljaard 1958, 1972; Howard and Washington 2019). Dry air is found to the west of this dryline, because the western interior of subtropical southern Africa is climatologically much drier than the east, containing the Namib and Kalahari Deserts as well as the Karoo semidesert farther south. Moist air east of the dryline mainly originates from the easterly trade wind regime, particularly when migratory highs ridge up on the east coast of South Africa (Ndarana et al. 2021). This dryline was referred to by Howard and Washington (2019) as the Kalahari discontinuity (KD), which they found to occur most often in November and December.

In a pioneering study on air masses in the South African region, Taljaard (1958) described the KD as a moisture front

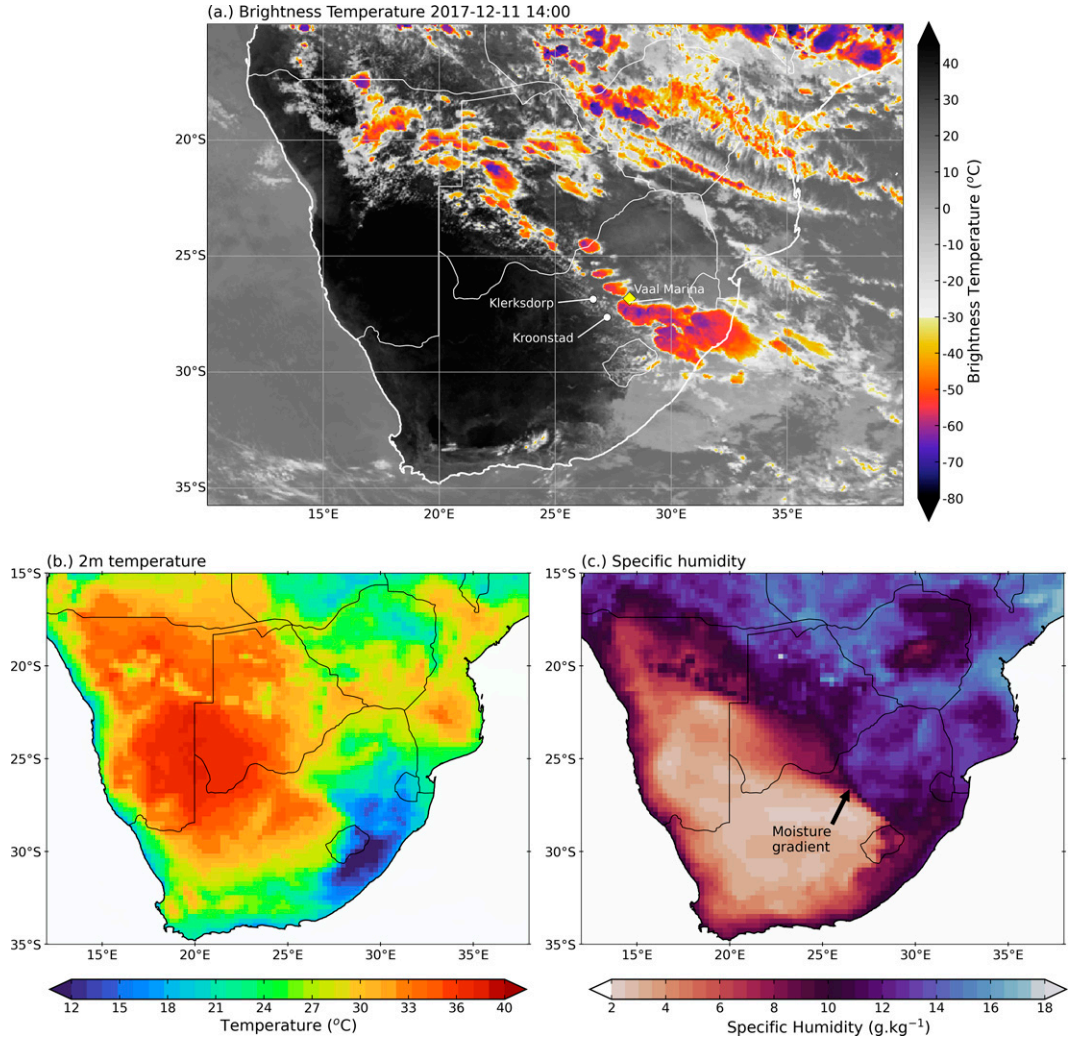

FIG. 2. (a) Brightness temperature (shaded; °C) at 1400 UTC 11 Dec 2017, taken from the MSG satellite (IR10.8 channel), showing convection developing to the west of the Vaal Marina. The ERA5 (b) 2-m temperature (shaded; °C) and (c) surface specific humidity (shaded; g kg^{-1}) at the same time/date as in (a) and showing the strong moisture gradient on the day where the convection originated. The locations of the two stations (Klerksdorp and Kroonstad) used in Fig. A1 in the appendix are shown in (a).

with no marked temperature discontinuity in most parts, but along which dewpoint temperatures change sharply. He noted that thunderstorm development occurred preferentially parallel and within 300 km on the moist side of the dryline. These thunderstorms would often develop into squall lines that could travel hundreds of kilometers and contribute significantly to summer rainfall. De Coning et al. (2000) and De Coning and Adam (2000) linked the presence of drylines over the interior of South Africa with severe thunderstorms, producing large hail and tornadoes on several occasions. Local weather forecasters have associated an enhanced potential for organized convection when a dryline is present (De Coning 2011; Thema 2013; Rae 2014; Lekoloane et al. 2021). For example, on 11 December 2017, a tornado associated with severe convection destroyed parts of Vaal Marina in South Africa (Fig. 2a), resulting in multiple casualties and the displacement of over 1000 people. A key feature associated with the development of the convection was a diagonal dryline running through the interior of South Africa and extending northwestward into Botswana (see Figs. 2b,c). A brief discussion of the evolution of this case is given in the appendix.

The characteristics of the air masses found over subtropical southern Africa as well as the moisture fluxes over this landmass are strongly influenced by the presence of the neighboring southern Indian Ocean and South Atlantic Ocean together with the topography (Fig. 1b). The latter is dominated by a continuous escarpment that separates the coastline from an elevated plateau (Fig. 1b). The escarpment comprises mountain ranges with elevations between 1000 and 2000 m, although the Drakensberg Mountain range, which forms part of the eastern escarpment, contains the highest mountain peaks in southern Africa, with elevations close to 3500 m. For

most of subtropical southern Africa, the escarpment lies close to the coastline, but it moves substantially farther inland for the Mozambican coast.

Apart from the south coast and nearby interior, which is an all-year rainfall region, and the extreme west and southwest, which receives rain in winter, southern Africa is predominantly a summer rainfall region (Taljaard 1996; Weldon and Reason 2014; Engelbrecht et al. 2015). Once the tropical rain belt has reached its maximum southern extent over central Mozambique and southeastern Zambia and starts to retreat equatorward during late summer, the subtropical high pressure belt shifts equatorward, allowing the intermittent landfall of cold fronts, causing rain mainly in the southwest (Reason et al. 2006). A continental high is established over the South African interior in winter, which together with the westward extension of the south Indian Ocean anticyclone keeps most of subtropical southern Africa dry except the far southwest. During summer, this high pressure region over the interior is replaced by a weak heat low that is linked by a trough across the Northern Cape province and Botswana to a tropical low north of Botswana (Munday and Washington 2017). Depending on moisture availability, thunderstorms develop to the east of this surface trough. Rainfall in summer is mainly convective (Gijben 2012) and can stem from isolated single-cell thunderstorms to organized mesoscale convective systems such as squall lines and mesoscale convective complexes (Blamey and Reason 2012). Tropical–extratropical cloud band systems (Hart et al. 2013) and continental tropical lows (Webster 2019) are also large contributors to the mean summer rainfall and to rainfall extremes over the interior (Malherbe et al. 2012; Howard et al. 2019; Rapolaki et al. 2019).

In their study of southern African drylines, Howard and Washington (2019) investigated the CAB and KD between August and December and showed that the CAB season is relatively short (August–October) and that, whereas CAB frequencies started to decrease after October, KD frequencies started to increase, reaching a peak in December. However, Howard and Washington (2019) did not investigate climatological characteristics of the KD during the rest of summer (January–March), which is typically wetter than the early summer. Here, drylines over subtropical southern Africa are investigated throughout the entire summer half of the year using 3-hourly ERA5 reanalysis data. To do so, we modify the Howard and Washington (2019) automated dryline detection algorithm as explained in section 2. The resulting climatology provides a detailed description of the monthly, seasonal, and interannual variability of drylines in subtropical southern Africa.

2. Data and method

a. Input data

ERA5 reanalysis data (Hersbach et al. 2018) were used to determine the characteristics of drylines in southern Africa between 1979 and 2020. Reanalysis data offer the ability to seamlessly analyze atmospheric conditions over long periods of time for certain time slots (Parker 2016). This is especially helpful over regions with few surface observations, which is the case for parts of the study region, mainly outside South Africa. Where surface observations are scarce, reanalysis data are often preferred for dryline climatological studies (Akter and Tsuboki 2017; Bechis et al. 2020). Here, ERA5 is available hourly at a grid spacing of 0.25° at 37 pressure levels between 1000 and 1 hPa. Surface specific humidity q, calculated from ERA5 2-m dewpoint temperature and surface pressure, was chosen as moisture parameter for the analysis since it is not affected by heating, cooling, or pressure changes (Stull 2017) and is conserved despite altitude changes. For the construction of the climatology, drylines were analyzed at 3-hourly intervals through the diurnal cycle.

Surface observations of temperature, dewpoint temperature, and pressure were obtained for the period from 2010 to 2019 for nine AWS stations in South Africa and Namibia to calculate specific humidity q. These data were for the most part available at 3-hourly time intervals, but between 2000 and 2013 data for certain stations were only available at the main synoptic hours (0000, 0600, 1200, and 1800 UTC). To ensure a good comparison across the years, the timeslots 0300, 0900, 1500, and 2100 UTC were excluded from the analysis when comparing ERA5 with the stations.

b. Dryline climatology

In this study a dryline is defined as a surface moisture boundary with a specific humidity gradient of at least 3 g kg^{-1} (100 km)$^{-1}$ with moisture gradient directions between 0° and 135° and a temperature gradient that deviates 90° or more from the moisture gradient for at least one-half of the dryline length. The temperature criterion is added to the definition to ensure that warm air is always west of the dryline and cooler air is always east of the dryline, thus preventing moisture boundaries associated with cold fronts from being detected. Cold fronts are relatively rare as the summer progresses and have cool air on the dry western side and warm air to the east.

All drylines are moisture boundaries, but not all moisture boundaries are drylines. Moisture gradients can be caused by topographical intrusions, thunderstorm outflow boundaries, cold fronts, and even soil moisture differences (Pielke and Segal 1986). In our study, the focus is on synoptic-scale drylines with a northwest–southeast orientation, as first described by Taljaard (1958), separating a moist air mass to its east from a dry air mass to its west, since these are most important for the climate of the region and potential severe weather development.

To objectively identify these drylines, the Canny edge detection method, which is described in detail by Howard and Washington (2019), was used. This method is applied to surface q fields to determine moisture gradients of 3 g kg^{-1} (100 km)$^{-1}$ or more. Hoch and Markowski (2005) first used this moisture criterion for dryline identification for a dryline climatology for the U.S. Great Plains region. Subsequently, this criterion was used in dryline studies elsewhere such as Argentina (Bechis et al. 2020), southern Africa (Howard and Washington 2019), and Australia (Arnup and Reeder 2007).

Figure 3 summarizes how a single dryline is detected for a particular timeslot on 5 January 2019. If the dryline identification

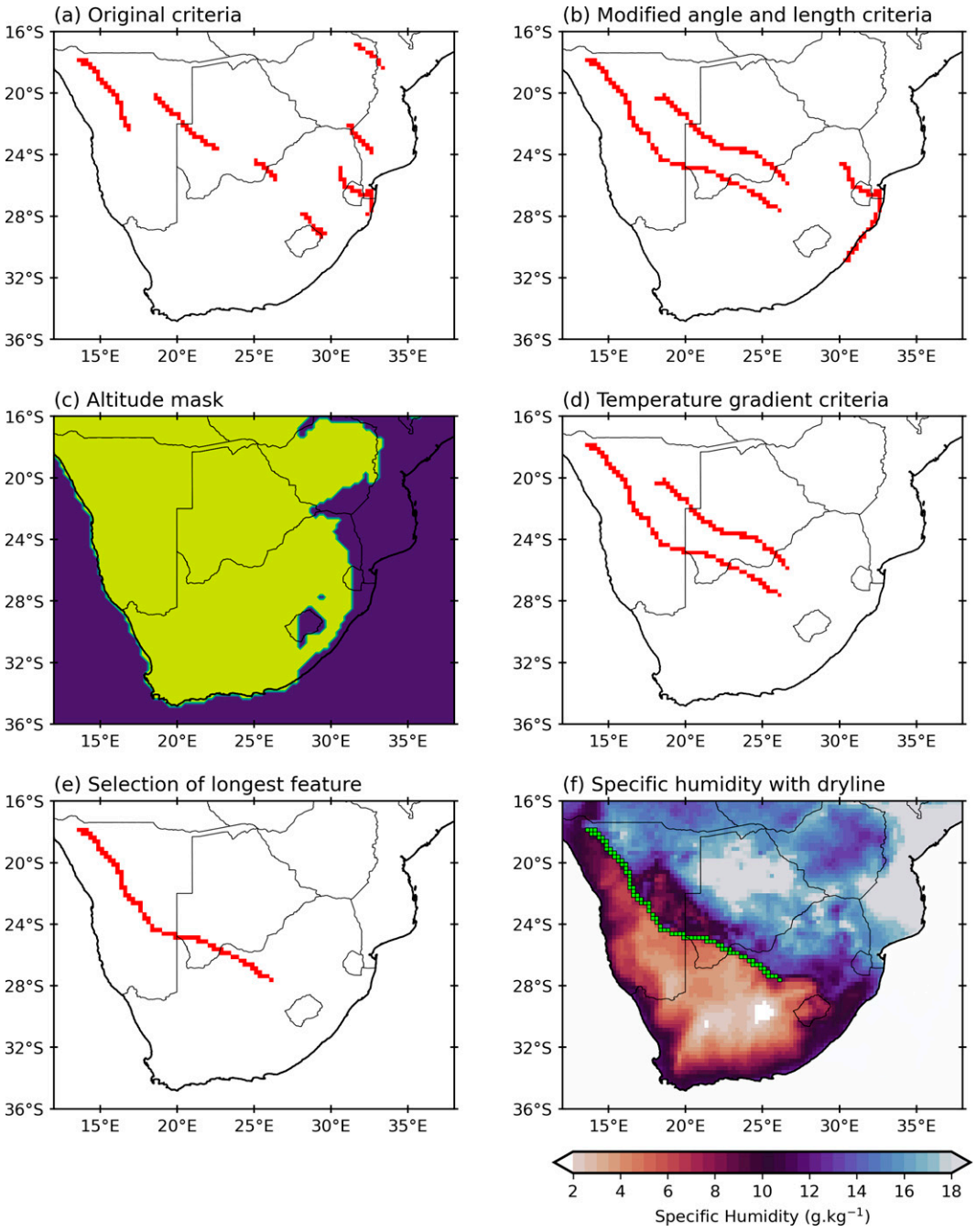

FIG. 3. An example of how the different steps (see the text) of the automated dryline detection algorithm function. We see (a) first all features detected by the Howard and Washington (2019) algorithm on 5 Jan 2019 and then (b) the new features identified after introducing the modified *angle* and *length* criteria. (c) The land/altitude mask used to remove features that occur over steep topography or flat coastal regions. (d) The features retained after introducing the *orientation of the temperature gradient* (i.e., to remove cold fronts). (e) Only the largest synoptic feature for the day is retained. (f) The dryline is identified (green line) using this method with surface specific humidity in the background (shaded).

method used by Howard and Washington (2019) is applied, then several features are detected, some of which appear to be unrealistic—for example, the one following the east coast near 26°–29°S (Fig. 3a). To connect sections of the same synoptic-scale dryline that the original method shows as separated, the moisture gradient angle filter was modified (Fig. 3b). Then a topography mask, temperature gradient, and minimum length criteria were applied (Figs. 3c–e)

to eliminate moisture boundaries that were not drylines. These steps are detailed below.

1) ORIGINAL CRITERIA

The orientation of the specific humidity gradient vector is determined for each grid cell after which gradients are filtered to only capture moisture gradients within specified thresholds. However, the requirement in Howard and Washington (2019) of only retaining grid cells that satisfy the moisture gradient criterion for gradient vector directions θ_q lying between 30° and 90°, relative to true north resulted in the capturing of small segments of synoptic-scale drylines (Fig. 3a). For this reason, additional criteria were modified and are outlined below.

2) MODIFIED ANGLE AND LENGTH CRITERIA

From daily weather operations, it is known that drylines in southern Africa generally have a northwest–southeast orientation (Taljaard 1958). Widening θ_q accordingly, so that any features with θ_q between 0° and 135° were retained, was the most successful approach in capturing entire drylines (Fig. 3b). The wider-angle filter, however, resulted in the capture of multiple moisture gradients that were not drylines. To address this problem and to ensure that only synoptic-scale features were captured, drylines were required to have a minimum length of 30 grid cells, which translates to around 750 km. Semipermanent moisture gradients caused by topographical features such as the Witwatersrand ridge over southern Gauteng (GAU) and eastern Northwest (NW) province (Fig. 1b) were thus eliminated. This criterion also removed moisture gradients that formed in the same location as the exit regions of the Limpopo and Zambezi low-level jets (LLJs). The Limpopo and Zambezi River valleys act as important moisture export regions, transporting water vapor from the southwestern Indian Ocean to the central interior of southern Africa via the Limpopo and Zambezi LLJs (Barimalala et al. 2021; Spavins-Hicks et al. 2021).

3) LAND AND ELEVATION MASK

Mountain ranges in the east and the east coast itself caused stationary surface moisture gradients that were observed regardless of the time of day. Therefore, all data at elevations below 700 m and above 1800 m east of 28°E were masked out. This process eliminates coastal effects and allows a focus on drylines over the subtropical interior plateau (SAP; i.e., south of 16°S), which are the subject of this study.

4) TEMPERATURE GRADIENT

Then the angle between the 2-m temperature gradient vector ∇T and specific humidity gradient vector ∇q must be greater than 90° for at least half of the grid cells within the dryline. Adding this step proved to be essential, not only for removing small segments that are not true drylines (Fig. 3d), but also for removing cold fronts, which have tight moisture and temperature gradients but in the opposite directions to drylines in South Africa. Note that climatological studies of drylines elsewhere in the world have used moisture gradient criteria in conjunction with temperature gradient criteria (Schaefer 1974; Schultz et al. 2007; Bechis et al. 2020) or wind direction criteria (Rhea 1966), or all three (Duell and Van Den Broeke 2016).

5) SELECTING THE LONGEST DRYLINE FEATURE

While the inclusion of temperature gradient criteria successfully removed cold fronts, other sources of moisture gradients still occurred occasionally, such as thunderstorm outflow boundaries. The final step in the process is to isolate a single dryline in the SAP domain per timeslot. Python image processing using the OpenCV Python package is used to select the longest line from moisture gradients that were not eliminated during the ∇T and ∇q differencing (Fig. 3e). The resulting dryline that adheres to all criteria listed above is then captured for analysis (Fig. 3f).

c. *Dryline characteristics*

Examination of the SAP drylines produced by the above method (e.g., Fig. 3f) shows that almost all pass through the 26°S latitude. Hence, this latitude line was selected to form the basis of all analyses of dryline characteristics such as seasonality, diurnal variability, persistence, onset time, and movement. In addition, 26°S passes through a region previously identified as a potentially severe convective environment during early summer (Blamey et al. 2016).

Three subsections were defined across the SAP at 26°S on the basis of their climatological characteristics. These are SAP-West (SAP-W; 18°–22.25°E), which shows a high frequency of summer dry spells (Thoithi et al. 2021) and late-summer (February/March) peak rainfall (Taljaard 1996; Tyson and Preston-Whyte 2000), and SAP-East (SAP-E; 24.75°–29.0°E), which has the opposite characteristic of low frequency of summer dry spells on average as well as an earlier peak in rainfall amount (December). Between SAP-W and SAP-E lies SAP-Transition (SAP-T; 22.5°–24.5°E), which is a zone characterized by a sharp gradient between dry and wet spells and where commercial farming changes from mainly livestock to maize as the rainfall increases eastward (Thoithi et al. 2021). SAP-E forms part of a potentially severe convective environment (Blamey et al. 2016) where tornadoes occur occasionally, as seen in the Vaal-Marina tornado case. Furthermore, it passes through the most densely populated province in South Africa, Gauteng, which is prone to severe thunderstorms during the summer half of the year that often lead to loss of life and severe damage to infrastructure and crops. Given the societal vulnerability along SAP-E, the interannual variability of drylines here and their associated circulation patterns are investigated through composite analyses of high- and low-dryline summers.

d. *Dryline lifespan and track*

Consecutive time steps, where a dryline intersected 26°S within the SAP, were defined as a dryline event. Events could span multiple calendar days. Dryline persistence is determined by counting the number of 3-hourly time steps for

each event. The dryline tendency to track eastward or westward is determined for each event by subtracting the dryline longitude at the final time step from the longitude of the first time step. This results in a positive value for an eastward-moving dryline and a negative value for a westward-moving dryline or zero when the drylines remained stationary.

e. *ERA5 and station data comparison*

To show that the ERA5 data used in the dryline detection adequately represent conditions over the SAP, nine AWS were selected that span the SAP in an east–west direction along three lines (Fig. 1b). The northernmost line lies between Windhoek and Gobabis in Namibia, where the highest occurrence of drylines was observed in ERA5 (detailed in section 3). The second line between Mahikeng and Irene extends across the Northwest and Gauteng provinces in South Africa while the southernmost line is between Pofadder and Bloemfontein (Fig. 1b). This selection of stations allows an intersection of drylines at different latitudes over the SAP, where they have been observed and documented before (Taljaard 1958; Howard and Washington 2019). Along each line, the selected stations were required to have data availability >75% and to be roughly 200 km apart. Using the Schultz et al. (2007) method to calculate dryline intensity using dewpoint temperature measured at individual stations, the specific humidity gradient was determined between adjacent stations by subtracting the eastern station value from the western station. The result was then normalized by dividing the specific humidity difference by the distance between stations and multiplying by 100 to obtain the specific humidity gradient (g kg^{-1} 100 km^{-1}) for adjacent station combinations (Fig. 1b). Drylines obtained using the objective identification algorithm described in section 2b were counted between the same station intervals. Days with drylines were matched with station moisture gradients that exceeded values of 3 g kg^{-1} 100 km^{-1} and were considered for analysis.

3. Results

a. *Seasonality of drylines on the SAP*

On average between 1979 and 2020, drylines on the SAP first occur in substantial numbers in September and steadily increase through the early summer (Fig. 4). During November–January, they occur almost daily (average of at least 25 drylines per month). This result compares well to that of Howard and Washington (2019), who found the KD to be present 100% of the time in November and December. Drylines peak first in SAP-E during November, followed by SAP-T and SAP-W, showing peaks in December. Dryline occurrence decreases gradually during late summer with very few cases on average during the dry winter months (May–August).

1) MOISTURE TRANSPORT AND DRYLINE LOCATION

Figure 5 shows the spatial distribution of all the drylines that occurred at 1800 UTC during the study period. This time was chosen since it is when drylines occurred most frequently on the SAP (discussed in section 3).

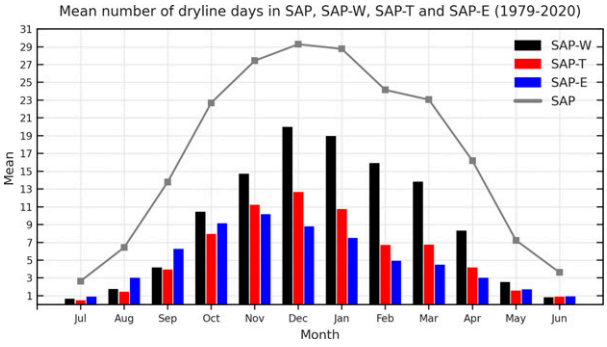

FIG. 4. The monthly average frequency of drylines detected over the southern Africa plateau (SAP), SAP-W, SAP-T, and SAP-E for 1979–2020. Note that the mean number of dryline days for each subsection does not add up to the mean number of dryline days on the SAP: if a dryline was observed in multiple subsections at different time steps of the same day, a dryline day was recorded for each subsection.

The spatial extent of drylines and the seasonal cycle is closely related to moisture transport patterns in southern Africa. Drylines start to occur more frequently in September, when low-level easterlies over Mozambique and Zimbabwe start strengthening with a northeasterly flow over northern South Africa/southeastern Botswana (Fig. 6a). During October and November (Figs. 6b,c), this northeasterly moisture flux increases, transporting moisture from the tropical south Indian Ocean over the eastern SAP (Figs. 7b,c). From January to March (Figs. 6e–g) the easterly moisture flux over southern Mozambique becomes southeasterly as a result of the development of the "Mozambique channel trough" (MCT) downstream of the Madagascan mountains as the Mascarene high retreats farther southeast over the subtropical south Indian Ocean (Barimalala et al. 2018, 2020). The southeasterly flow is channeled through the Limpopo Valley by the Limpopo LLJ, resulting in a northeasterly flow into Botswana (Spavins-Hicks et al. 2021). The importance of the LLJ for transporting moisture over the SAP has been confirmed in regional WRF experiments (Barimalala et al. 2021). From December (Fig. 6d), a secondary moisture source is evident from the tropical southeastern Atlantic Ocean feeding into the Angola low (Mulenga et al. 2003; Cook et al. 2004), which is a tropical low that started off as a heat low in early summer (Munday and Washington 2017) over the southeastern Angolan/northeastern Namibian region. The Angola low is often the source region for the tropical–extratropical cloud bands that contribute substantially to summer rainfall over the SAP (Hart et al. 2010, 2013).

Together, the northerly flux around the Angola low and the Limpopo LLJ driven easterly flux result in moisture increases over the western SAP from December to March (Figs. 7d–g). The Angola low weakens and moves northward in March and by April is no longer evident (Figs. 6g,h). At the same time, the Mascarene high moves back toward southeastern Africa, the Limpopo LLJ weakens, the MCT weakens and disappears, and there is increasing subsidence, less surface

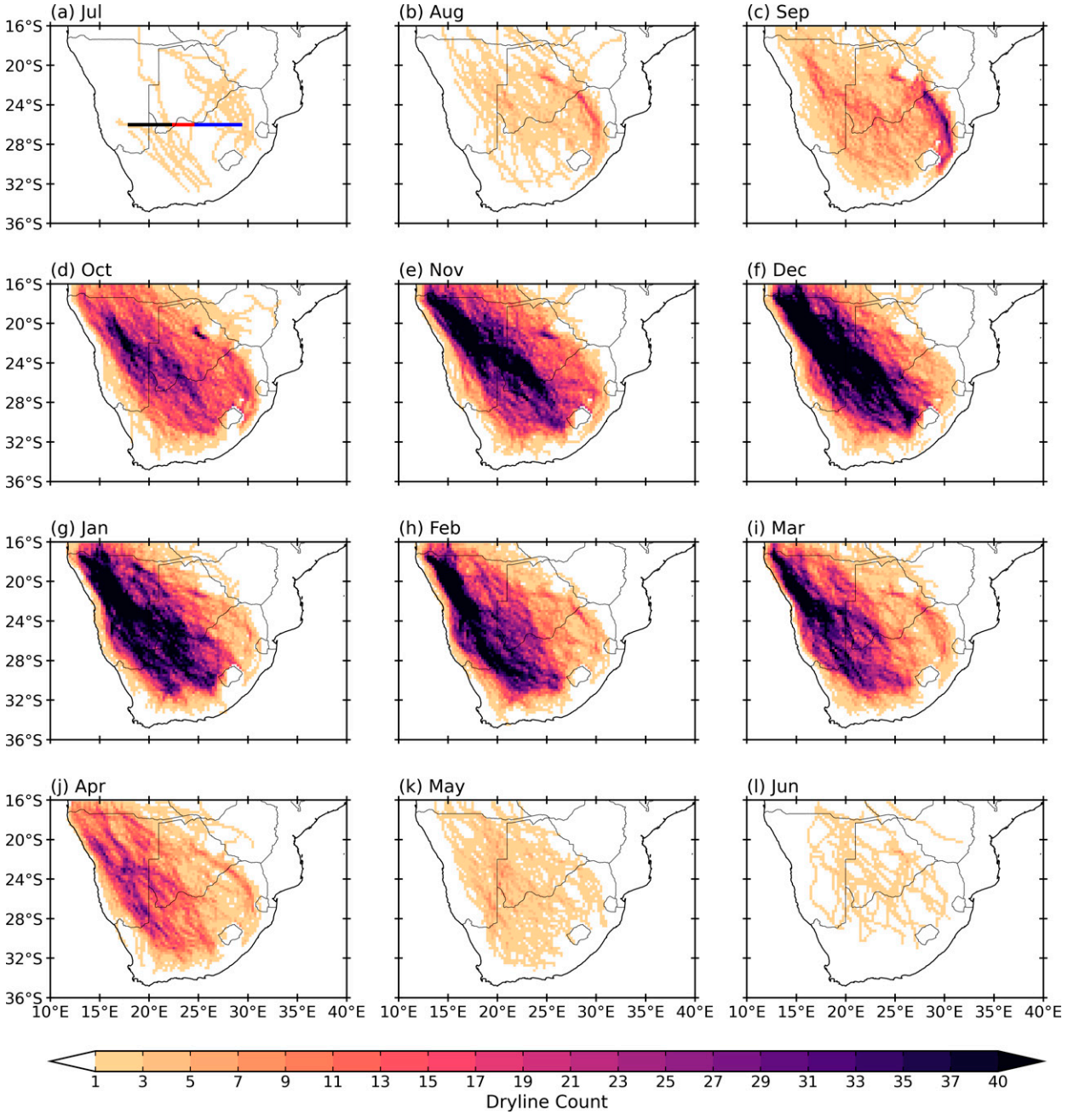

FIG. 5. The monthly spatial distribution of drylines detected at the 1800 UTC time step by the objective dryline detection algorithm applied to ERA5 data.

moisture (Fig. 7h), and less rainfall on average over subtropical southern Africa than in December–February. In general, this seasonal cycle in moisture transport results in moisture availability over the eastern parts of southern Africa being highest during the late summer months of January and February.

This monthly evolution of low-level moisture flow over southern Africa provides insight into the spatial variations in the frequency of drylines on the SAP throughout summer seen in Fig. 5. Drylines occur most frequently during November, December, and January with an obvious maximum over western southern Africa during these months (Figs. 5e–g). Dryline occurrence simultaneously starts to decrease over the eastern SAP after November. Concomitant with the steadily increasing influx of moisture from the east coming from the south Indian Ocean, SAP drylines peak at different times in summer. An analysis of drylines that transected the 26°S latitude of the SAP indicates that for SAP-E, drylines occur most

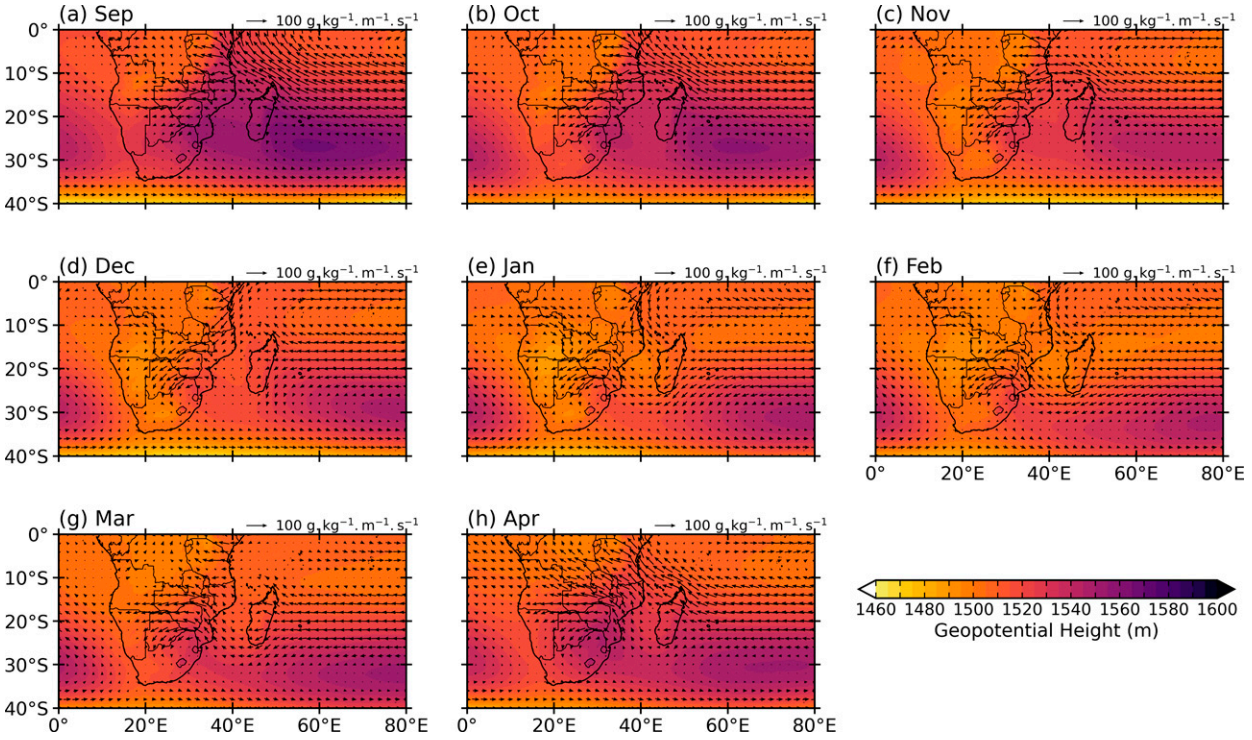

FIG. 6. The monthly mean ERA5 850-hPa geopotential height (shaded; m) and moisture flux (vectors; g kg^{-1} m s^{-1}) during the austral summer months from (a) September through to (h) April, as derived from the monthly ERA5 reanalysis over the period 1979–2020.

often in November, whereas farther west on the SAP-W transect the peak is shifted to December (Fig. 4) as the interior heats up and more moisture is transported from the east into the Kalahari heat low. The latter acts as the western boundary to which moist air can penetrate from the Indian Ocean (Taljaard 1986).

The lowest number of drylines with a northwest–southeast orientation occurs over northeastern Botswana and Zimbabwe. However, drylines with a west–east orientation were detected frequently there during December, January and February (DJF) during the testing phases of the dryline detection algorithm (not shown). Further analysis indicated that the algorithm was in fact detecting the dryline on the southern edge of the southward-migrating tropical rainbelt (J. G. Chabata, former Zimbabwean forecaster, 2021, personal communication). The highest occurrence of drylines for all 3-hourly time steps was found to extend from northwestern Namibia southeastward across southwestern Botswana and the northeastern parts of the Northern Cape province in South Africa (Kalahari Desert) (Fig. 5f). During December and January, a semipermanent heat low (Kalahari heat low) (Taljaard 1986; Munday and Washington 2017) develops here, which is also partially visible at 850 hPa in Figs. 6d and 6e.

2) MOISTURE GRADIENTS IN STATION DATA

In their study of the KD, Howard and Washington (2019) used surface observations to establish that the KD is a feature of the true atmosphere and not a reanalysis artifact, by investigating changes of weather conditions before and after the passage of a dryline. In our study, moisture gradients exceeding 3 g kg^{-1} 100 km^{-1} were determined between AWS spanning across the SAP in various locations (A–F in Fig. 8c). A direct comparison between ERA5 drylines and AWS moisture gradients between these locations showed a much lower occurrence of moisture gradients that satisfy the 3 g kg^{-1} 100 km^{-1} criterion than ERA5 drylines (Fig. 8b). This difference is most likely not a result of reanalysis error but rather is a result of the distance between adjacent stations leading to an underestimation of moisture gradients in some cases. Nevertheless, there are similarities between the two graphs in Fig. 8b. Troughs and peaks between the drylines and moisture gradients generally align, except between Pofadder and Upington in ERA5 drylines, where, instead of a peak seen in the stations, a slight drop was observed during February. The longer reanalysis dataset (Fig. 8a), spanning over 42 years, also indicates a peak in the number of drylines between Pofadder and Upington during February. The mean number of moisture gradients and drylines remained relatively constant from December to March between Upington and Postmasburg (Fig. 8b), but the longer dataset (Fig. 8a) shows a drop in ERA5 drylines after December. The station data between Mahikeng and Irene show a peak in December, whereas the ERA5 drylines peak in November.

The shift in the peak location of drylines and moisture gradients through the summer is evident again in both the ERA5 and observation datasets (Fig. 8b). Over the eastern parts of

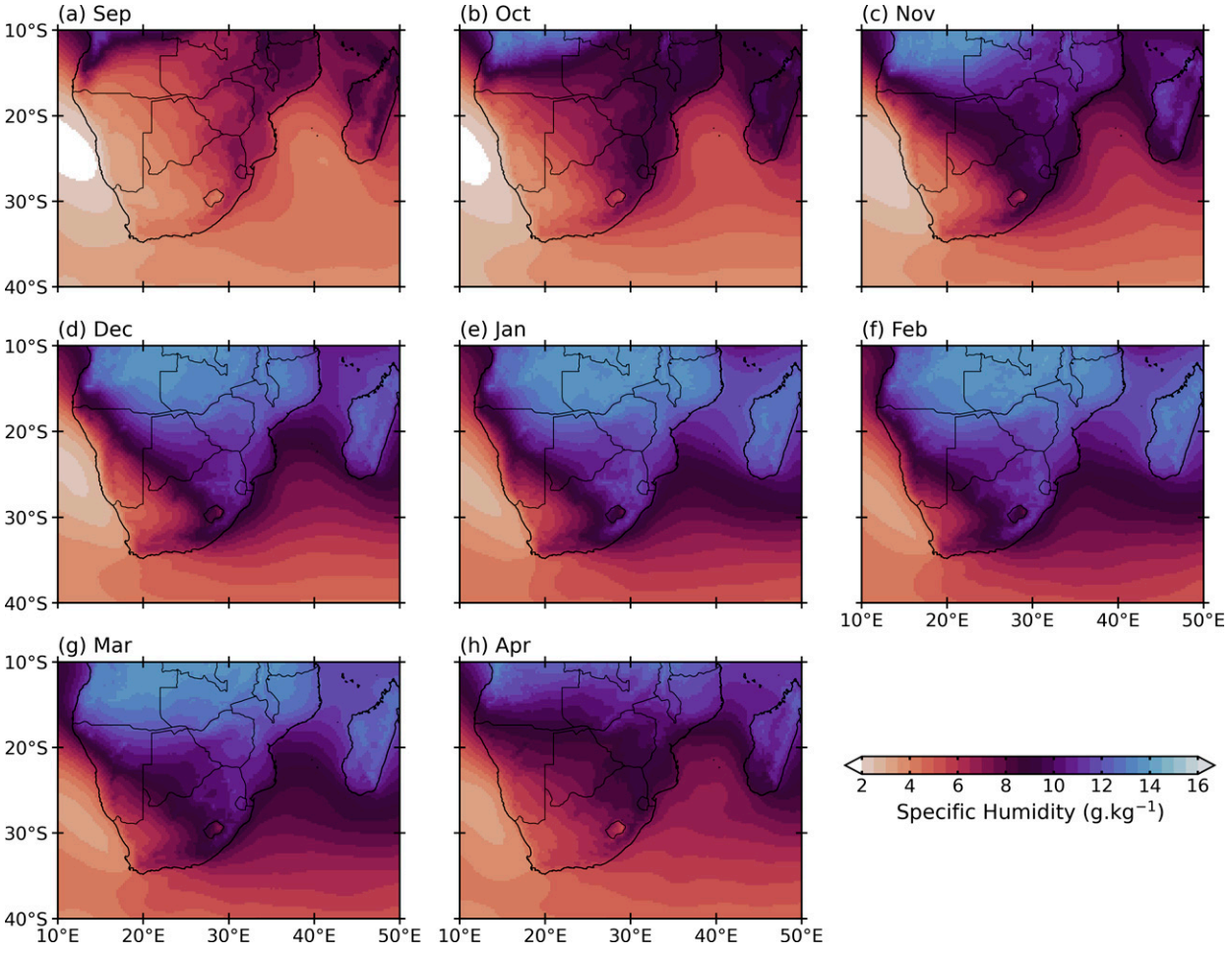

FIG. 7. The monthly mean of the 850-hPa specific humidity (shaded; m) from (a) September through to (h) April, as derived from the monthly ERA5 reanalysis over the period 1979–2020.

the SAP, dryline occurrence peaks in November between Mahikeng and Irene (A in Fig. 8a). Positioned centrally on the SAP, points D (Postmasburg and Kimberley) and E (Kimberley and Bloemfontein) peak in December, while the westernmost segments, Pofadder to Upington (C) and Upington to Postmasburg (D), show peaks in late summer (January–February). Similarly shaped curves of the AWS moisture gradients exceeding 3 g kg^{-1} 100 km^{-1} matched with ERA5 drylines between Windhoek and Gobabis (in Namibia) indicate a sharp increase until December, followed by a sharp drop in January (Fig. 8b). From December to February, this rapid decrease in the number of drylines east of Windhoek is captured well in Figs. 5f–h, while a simultaneous sharp increase in the number of drylines is visible west of Windhoek, suggesting a rapid westward shift in the location of drylines in Namibia toward the end of summer. This transition of moisture gradients in the SAP domain seen in the AWS data, with moisture gradients being more frequent in the east during the early summer and west during the late summer is consistent with the monthly evolution of the moisture fluxes described earlier in Fig. 6.

3) DIURNAL CHARACTERISTICS OF DRYLINES

Drylines on the SAP were detected most frequently in the evening, in the 1800 UTC (2000 LST) and 2100 UTC (2300 LST) synoptic time slots (Fig. 9a). Similarly, the highest frequency of AWS moisture gradients was observed at 1800 UTC (2000 LST), followed by 0000 UTC (0200 LST) (not shown). This is consistent with findings by Howard and Washington (2019) that KD moisture gradients during November were strongest at night and weakest at midday. Drylines on the central Argentinian plains had similar diurnal characteristics with peaks during the late afternoon (1500 LST) and evening (2100 LST) (Bechis et al. 2020). The northern Australian dryline also showed clear diurnal variation, intensifying during the night (Arnup and Reeder 2007). This timing is in contrast with drylines on the North American Great Plains, which tend to be strongest during the day and weakest at night (Schaefer 1986).

An analysis of the frequency with which drylines intersect the western versus eastern half of the SAP at 26°S shows that there is a peak occurrence of drylines at 1800 and 2100 UTC from December to March for SAP-W (Fig. 9b). Peak dryline

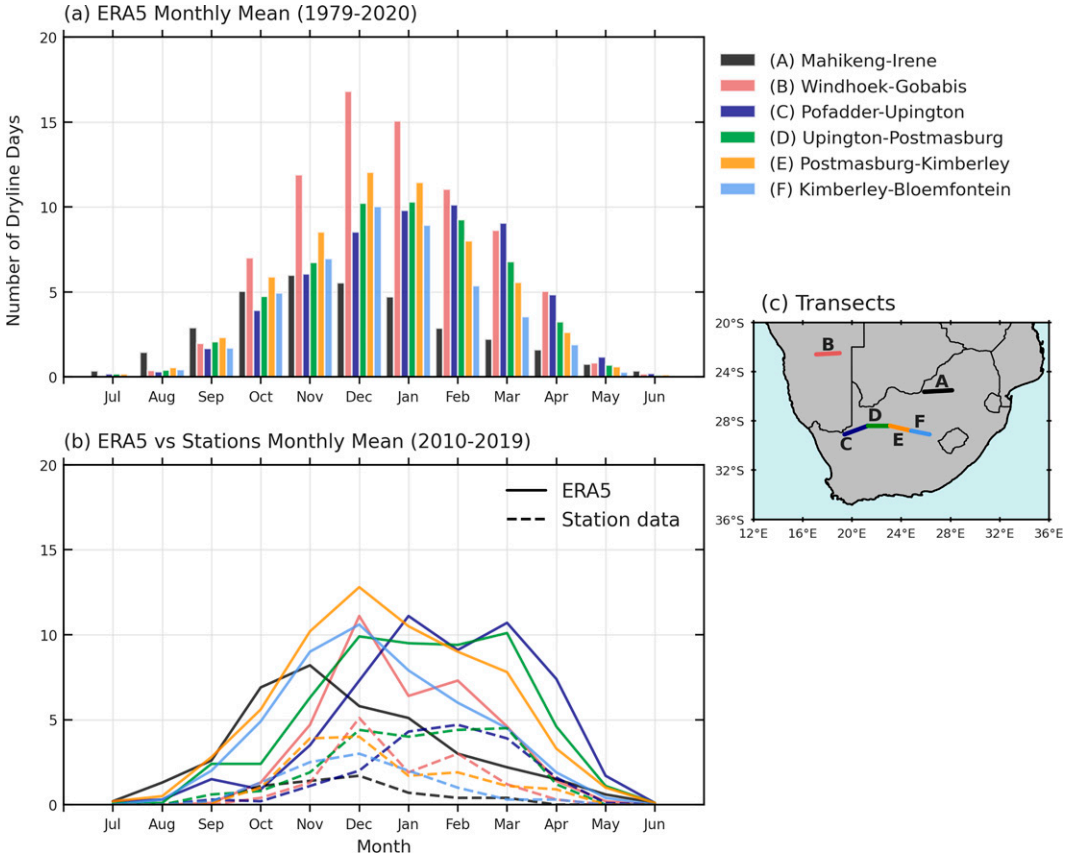

FIG. 8. (a) The seasonal cycle of drylines in ERA5 (1979–2020) detected between AWS locations spread across South Africa and Namibia [see the legend and (c) the insert]. The *y*-axis count is represented as the mean number of days for a given month that a dryline was detected at any time step between the different AWS. (b) The ERA5 dryline data (solid lines) in comparison with the mean number of days per month on which moisture gradients (dashed lines) exceed 3g kg^{-1} 100 km^{-1} between the different AWS segments for the 10-yr period 2010–19.

occurrence for SAP-E takes place during the afternoon (1200 and 1500 UTC) from November to February (Fig. 9d). Drylines rarely occur over the eastern SAP overnight and during the morning hours (0000, 0300, and 0600 UTC) but are more frequently observed at those times in the transition zone between the drier SAP-W and more humid SAP-E (Fig. 9c). Drylines in SAP-T occur more frequently than in SAP-E, despite being a smaller segment.

On the basis of 9474 dryline events between 1979 and 2020 that lasted at least 3 h and transected the 26°S line on the SAP, Fig. 10a plots the number of drylines whose onset occurred at the given time as a percentage of total dryline occurrence in each segment. Onset times for the different segments show similar characteristics with peak onset at 0900 UTC and lowest onset in the early morning hours of 0000 and 0300 UTC. Surface heating seems to play an important role during dryline formation for all segments, considering that onset times on the SAP coincide with the times of day (0900–1500 UTC) when surface temperatures start rising rapidly to their daily maximum in the early afternoon (not shown). The percentage distribution of onset times was similar for events that lasted longer than 6 or 9 h (not shown). SAP-W and SAP-T show a weak secondary peak in onset at 1800 UTC, which will be discussed at the end of this section.

In terms of duration, 43% of dryline events were observed for a single 3-h time step and 20% of events lasted two time steps. Longer events are rare, and only 2% of events were observed for eight consecutive time steps or more (a 24-h period or longer). Statistically there was no significant difference between the persistence of drylines in SAP-W, SAP-T or SAP-E, but drylines in SAP-W and SAP-T tend to persist slightly longer than drylines in SAP-E, which could explain their higher occurrence during evening hours (Fig. 9).

4) DRYLINE MOVEMENT

The net movement of all dryline events is shown in Fig. 11. On all three transects, but particularly on SAP-E, the majority of events (44%–56%) were essentially stationary. For the other cases, 27% tended to move westward and 28% tended to move eastward for SAP-W; 26% tended to move eastward and 30% tended to move westward for SAP-T; drylines had a larger tendency to move westward (29%) than eastward (15%) for SAP-E. Variability in onset times of dryline events

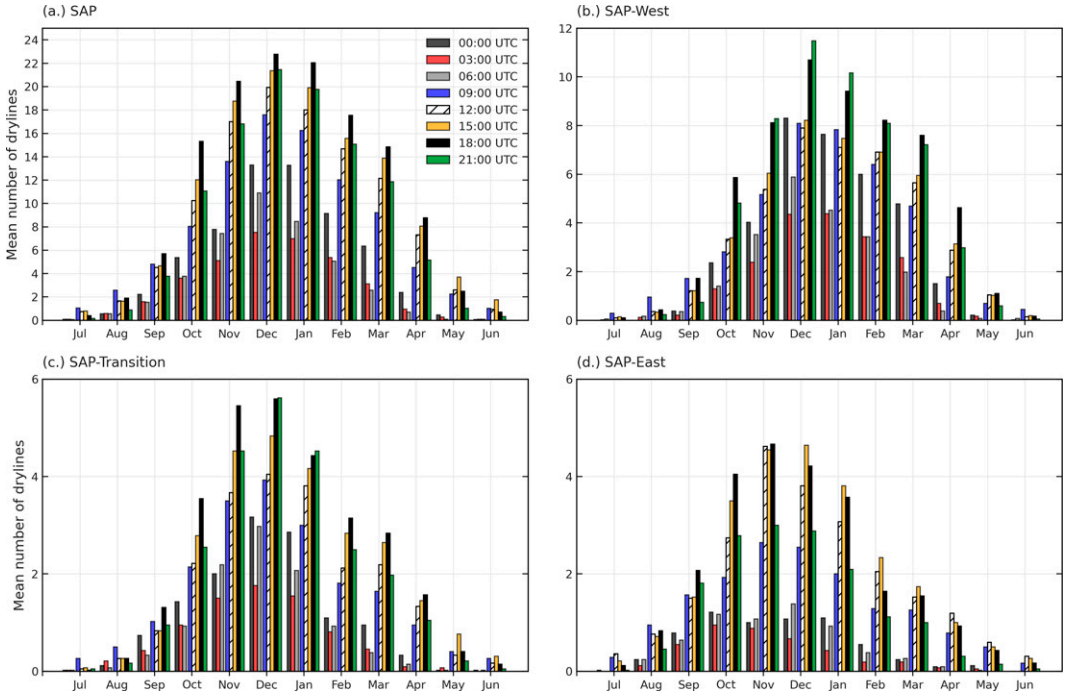

FIG. 9. Monthly mean of drylines detected in ERA5 (1979–2020) that intersect each segment along 26°S at the 3-hourly intervals between 0000 and 2100 UTC [see (a) for bar legend] for (a) the full 26°S transect, (b) SAP-W, (c) SAP-T, and (d) SAP-E (see Fig. 1a for locations).

became further apparent once events were divided into two groups on the basis of whether drylines moved eastward or westward (Figs. 10b,c). For all segments, westward-tracking drylines tended to have a later onset during the day, peaking between 1200 and 1800 UTC (Fig. 10b). On the other hand, eastward-moving drylines showed peak onset times at 0900 and 1200 UTC (Fig. 10c).

b. *Interannual variability and trends*

The annual number of dryline days across the SAP does not show much variation during the peak summer months (DJF). On average, 80 drylines occurred somewhere along the SAP 26°S line during DJF with a standard deviation of 4.5. The interannual variation on the full SAP line showed no significant correlation with the Niño-3.4 index. A Mann–Kendall test revealed no significant monthly or seasonal trends, except for an increasing trend for drylines on the SAP line during November (significance level $p = 0.005$) as well as for SAP-E during SON ($p = 0.005$). No significant relationships between dryline occurrence and the Southern Annular Mode were found.

Standardized anomalies in DJF dryline frequency on SAP-W, SAP-T, and SAP-E during the period are plotted in Fig. 12 along with the Niño-3.4 index. Typically, ENSO affects southern African rainfall most strongly in DJF, with weaker correlations in the earlier summer months (Reason et al. 2000).

DJF had the highest average number of dryline days (Fig. 4) as well as the largest interannual variability (Fig. 12a). Both SAP-T and SAP-E dryline frequencies are correlated at correlation coefficient $r > 0.4$ ($p < 0.05$) with the Niño-3.4 index (Fig. 12b). Thus, drylines on SAP-T and SAP-E tend to occur more often during El Niño summers when rainfall is typically well below average in most of subtropical southern Africa and less often during La Niña summers when rainfall is typically well above average in most of subtropical southern Africa. For SAP-E, the extreme cases of no drylines at all occurred during the strong DJF 1988/89 La Niña summer while maximum numbers (45 drylines) occurred during the 2018/19 El Niño. SAP-T also showed the least and greatest numbers during these two summers respectively. The strong 2000 La Niña summer also showed very few drylines on SAP-T and SAP-E. Although there is no significant relationship between ENSO and dryline frequency on SAP-W as a whole, if one considers only the western half of SAP-W, then a relatively weak but significant inverse correlation is found with the Niño-3.4 index ($r = -0.33$; p value $= 0.005$) This implies that more or fewer drylines tended to occur during La Niña or El Niño events, respectively, for the extreme western parts of the SAP. Taking note of the tendency of high-dryline years in SAP-W to be associated with low-dryline years in SAP-E (Fig. 12a), it is not surprising that there exists a negative correlation ($r = -0.43$; p value < 0.005) between dryline days in SAP-W and SAP-E. In general, variability in SAP-W dryline frequency tends to show smaller anomalies from 1996 to 2010 than either before or after this period.

Overall, SAP-T and SAP-E tend to vary more or less in phase with each other and indeed are strongly correlated ($r = 0.64$; p value $\ll 0.05$). One exception occurred during the very strong 1997/98 El Niño summer when dryline frequency

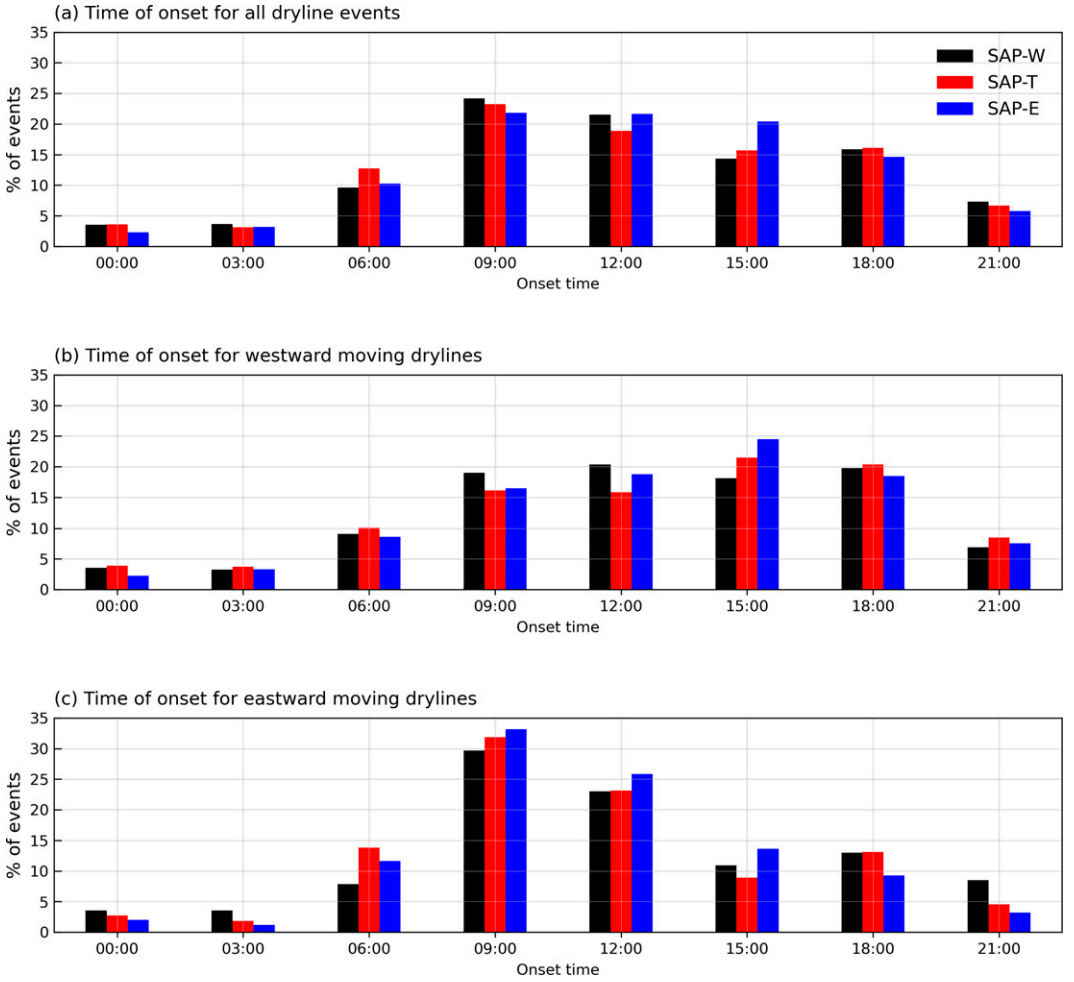

FIG. 10. The mean onset times (UTC) of all dryline events that (a) intersect the SAP at 26°S or show a net (b) westward or (c) eastward movement.

was unexpectedly average on SAP-E but well above average on SAP-T. A possible explanation could be that this El Niño event was characterized by anomalously wet conditions over Namibia and large parts of South Africa (Reason and Jagadheesha 2005), which is a more La Niña–like rainfall response. To further investigate dryline interannual variability during DJF, composites of specific humidity and circulation anomalies are determined for seasons with anomalously low (1988/89, 1999/00, 2007/08, 2010/11) and high (1994/95, 2003/04, 2015/16, 2018/19) dryline frequencies in SAP-E (Fig. 12a).

Figure 13a shows that summers with low dryline frequency along 26°S in NW and GAU provinces of South Africa (SAP-E) show statistically significant positive anomalies in specific humidity over not just the entire 26°S SAP transect but also large areas to its north, south, and west, thereby weakening the climatological moisture gradients near SAP-E, leading to low numbers of drylines. More or less the reverse pattern is found in the high-frequency composite (Fig. 13b). Relative to the climatology (Fig. 13c), low-dryline summers show stronger northeasterly moisture fluxes over the Kalahari heat low region in the Northern Cape and hence greater penetration of moisture farther west and southward leading to reduced moisture gradients and fewer drylines (Fig. 13d). On the other hand, moisture flux anomalies are southerly over the Northern Cape and southern Botswana during high-dryline years (Fig. 13e), leading to reduced penetration of moisture here, with stronger gradients and hence more drylines.

Summers with anomalously high drylines are characterized by a stronger Botswana high (Fig. 14a). This midlevel high leads to strong subsidence over the western half of subtropical southern Africa (Reason 2016), helping to keep that region drier than the east, and promotes the existence of strong moisture gradients near the surface across the SAP. Many El Niño summers are also ones of a stronger Botswana high (Driver and Reason 2017) consistent with Fig. 12a showing higher dryline frequencies in SAP-E and SAP-T during most El Niño summers. The increased subsidence in high- versus low-dryline summers is evident over virtually all the domain in the 500-hPa omega difference plot (Fig. 14b).

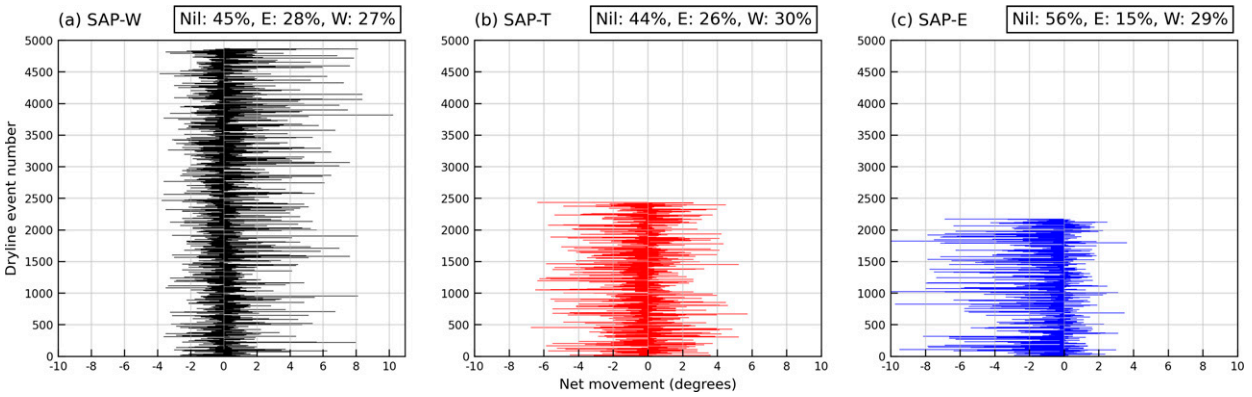

FIG. 11. The net movement of each dryline (from start) given in eastward (>0) or westward (<0) direction and in degrees of longitude for the three transects: (a) SAP-W, (b) SAP-T, and (c) SAP-E. The percentage of each class is provided at the top of each panel: "Nil" indicates the percentage of drylines of a total of 9474 events that were recorded for one time step only or remained stationary during its lifespan and "E" and "W" show the percentage of drylines that respectively had a net eastward or westward movement. The *y* axis indicates the event number of events that occurred in each segment.

A vertical section along 20°E highlights the role of the Botswana high, the Kalahari heat low, the Angola low (Fig. 15a), and composite anomalies during the low- and high-dryline summers (Figs. 15b,c). Since the interior plateau sits at 1–1.5 km above sea level, the transect extends up from the 850-hPa level. On average, the Botswana high is located over 20°–26°S with subsidence clearly evident in the 400–500-hPa level (Fig. 15a). Farther south is the tropospheric subsidence associated with the descending branch of the Hadley cell. Beneath the Botswana high is the low-level uplift (~23°–30°S) associated with the Kalahari heat low while farther north and particularly near 11°–18°S is the strong uplift through the troposphere associated with the deep convection of the Angola low. During low-dryline summers (Fig. 15b), there are low-level cyclonic

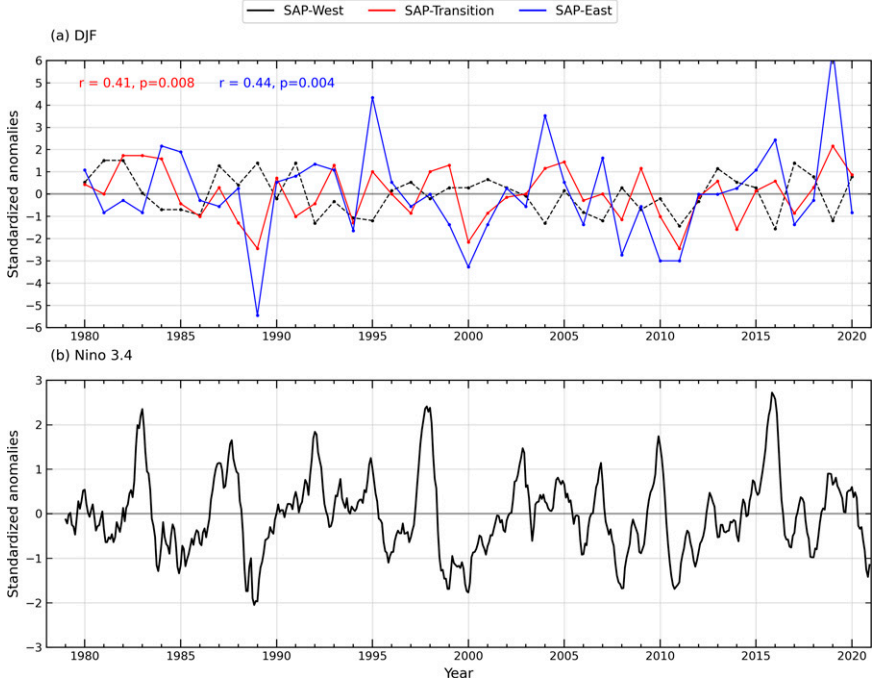

FIG. 12. (a) Total dryline count anomalies for SAP-W (black), SAP-T (red), and SAP-E (blue) transects during DJF for each year from 1979 to 2020 [significant correlations (and *p* value) with ENSO are indicated in the color of the respective segment] and (b) normalized monthly sea surface temperature anomalies for the Niño-3.4 region based on ERSSTv5 data (Huang et al. 2017) for the same period.

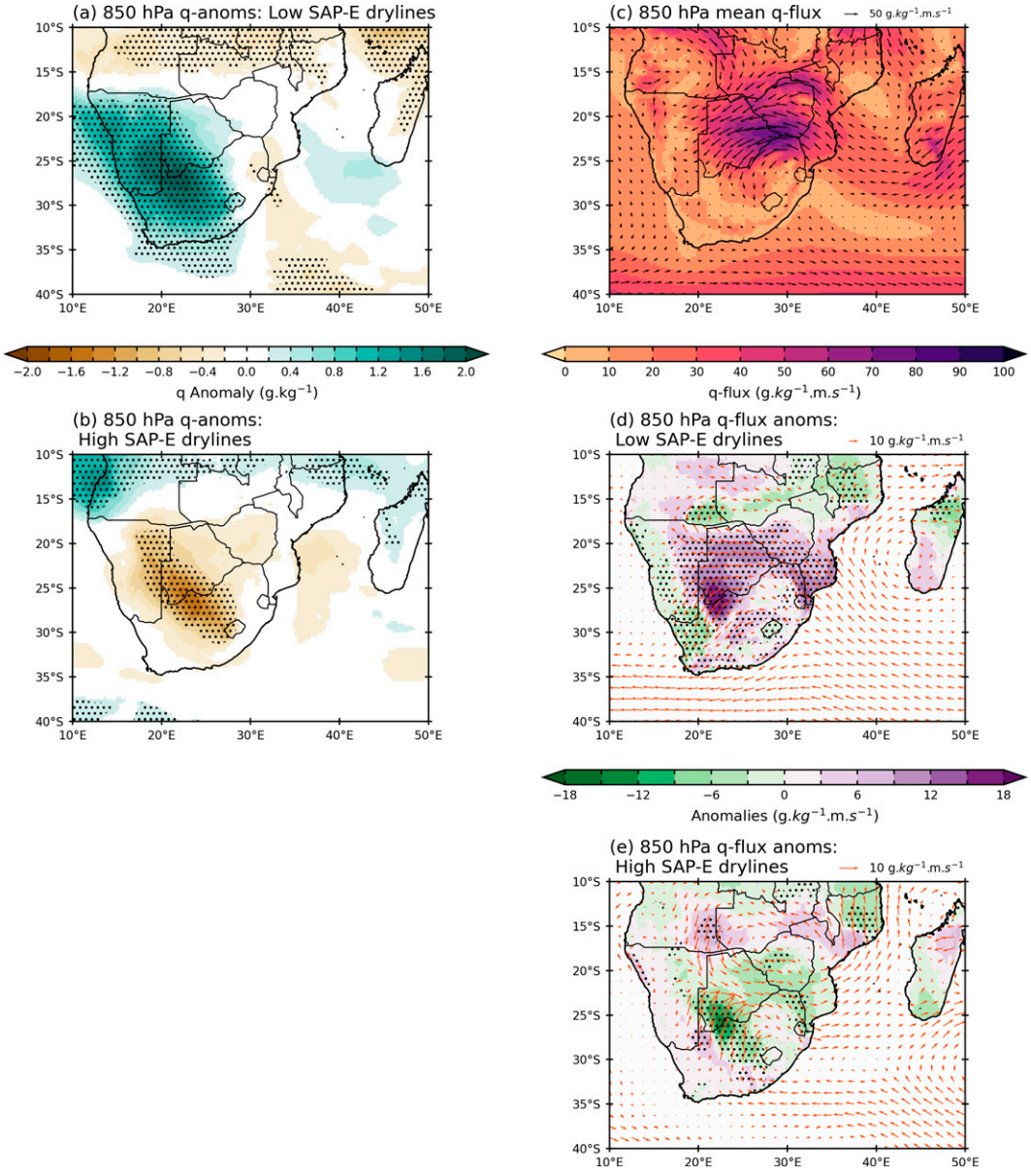

FIG. 13. Composite anomalies for 850-hPa specific humidity during (a) the four summers with lowest dryline counts for SAP-E (1988/89, 1999/2000, 2007/08, and 2010/11) and (b) the four summers with highest dryline counts in SAP-E (1994/95, 2003/04, 2015/16, and 2018/19). (c) Mean moisture flux and moisture flux magnitude (shaded) at 850 hPa for DJF. The mean is based on monthly ERA5 data from 1979 to 2020. Also shown are the 850-hPa composite anomalies for moisture flux magnitude (shaded) and moisture flux anomaly vectors during the SAP-E (d) low-dryline summers and (e) high-dryline summers. Stippling in (a), (b), (d), and (e) denotes values that are significant at or above 95% after applying a two-tailed nonparametric Monte Carlo bootstrap statistical significance test.

anomalies over southern Angola (Fig. 13d), a weaker Botswana high, a stronger Angola low and more uplift north of 18°S (Fig. 15b), and a southward shift in the Kalahari heat low together with more northwesterly flux into SAP-E, thus leading to fewer drylines. Roughly the reverse occurs during the high-dryline summers (Fig. 15c). The difference plot (high-dryline case minus low-dryline case in Fig. 15d) indicates that the strongest changes are at mid- to upper levels in the Botswana high and the southern half of the Angola low, and at low levels through 23°–30°S in the Kalahari heat low region.

4. Discussion and conclusions

A dryline climatology was presented for the subtropical southern Africa interior using an objective dryline identification algorithm and 3-hourly ERA5 reanalysis data. The

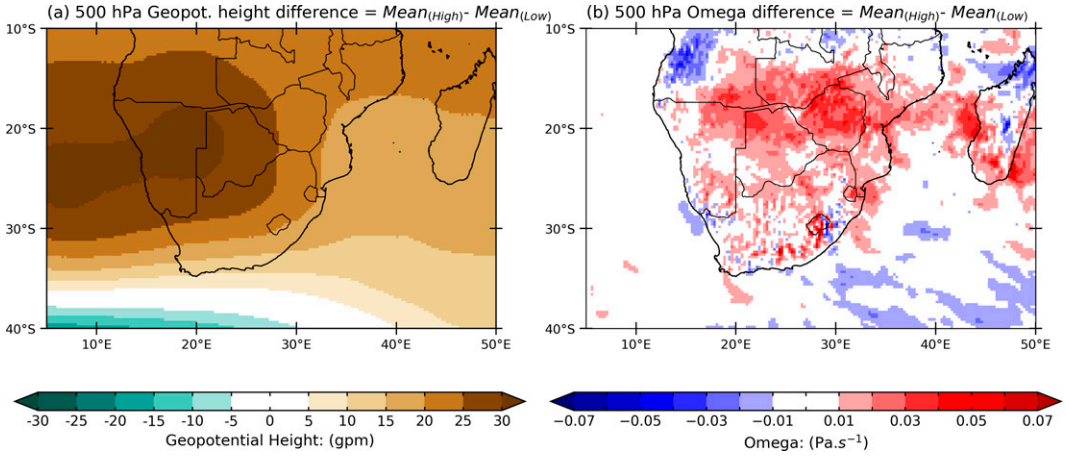

FIG. 14. Differences at 500 hPa between high (1994/95, 2003/04, 2015/16, and 2018/19) and low (1988/89, 1999/2000, 2007/08, and 2010/11) composites for (a) mean geopotential height and (b) mean omega.

seasonal cycle of drylines is tied to regional moisture transport patterns. Drylines occur frequently over the southern African interior in the austral summer and occur almost daily during December through to February. There is a clear spatial pattern evident in the seasonal cycle of drylines. Although there is a lower frequency of drylines that formed in the eastern part of the domain (SAP-E), they show a peak occurrence during spring (SON), decreasing after December. Over the central and western part of domain (SAP-T and SAP-W, respectively), dryline occurrence peaks in December and January before decreasing toward the end of summer (MAM).

Comparisons between AWS observations and ERA5 drylines across smaller subsections revealed the westward shift in greater detail, showing that peaks in dryline occurrence and specific humidity gradients occurred in November for stations in the east (transect A), December for central stations (transects E and F), January and February for western stations (transects D and C) (see Fig. 8 for locations). This westward shift in the peak of dryline occurrence during the course of summer

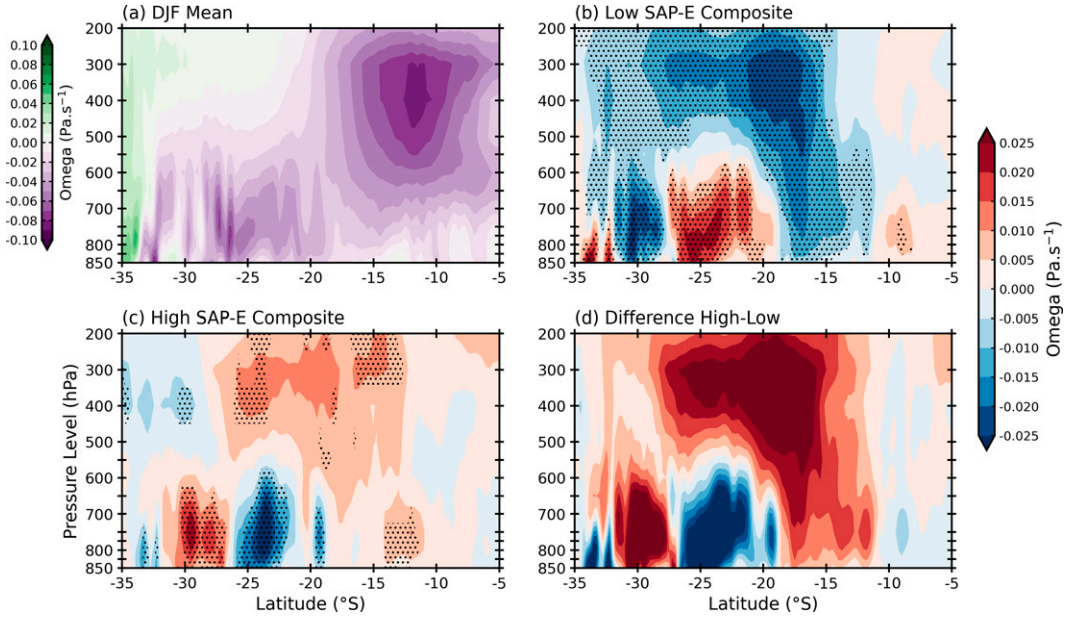

FIG. 15. (a) Vertical cross section (longitude is averaged across 18°–24°E) of the mean DJF omega (Pa s^{-1}) from 850 to 200 hPa. The 850-hPa surface corresponds to an approximate height of 1500 m, slightly higher than the height of average regional topography. Also shown is the composite anomaly of omega for years with (b) low dryline frequency and (c) high dryline frequency, along with (d) the difference between high and low. Stippling in (b) and (c) denotes values that are significant at or above 95% after applying a two-tailed nonparametric Monte Carlo bootstrap statistical significance test.

coincides with the westward increase of moisture flux penetrating the interior from the southern Indian Ocean and also the westward march of the 50 mm accumulated rainfall isohyet as described by Taljaard (1996).

Climatologically, the early summer months are the most favorable for the development of severe thunderstorms over eastern South Africa. The postwinter baroclinic state of the atmosphere is drier in the middle and upper troposphere with favorable wind shear values, but becomes moister with weaker shear during late summer (January–March) (Dyson 2015). Blamey et al. (2016) showed that potentially severe thunderstorm environment days over the interior of South Africa peaked during October and November with the highest frequency east of Gauteng. Eastern South Africa also has the highest hail day frequency during October–December (Dyson et al. 2021). Morake et al. (2021) found a peak of long-lived mesoscale convective systems over eastern South Africa in December. In this study, it was shown that drylines over the eastern interior peak during SON. Furthermore, an increasing trend was found for drylines in the SAP-E during SON. This suggests that drylines might be an important factor to consider in the severe thunderstorm environment over the region, and the relationship between dryline occurrence and thunderstorm development will be the focus of future work.

Differences in dryline characteristics between SAP-W and SAP-E suggest that different formation mechanisms are at play for drylines that form over the western interior versus those forming in the east. The westward-movement tendency of drylines in SAP-E, SAP-T, and SAP-W suggests that a moisture push from an easterly or northeasterly direction is involved, often enhanced by ridging of migratory anticyclones south of South Africa and along the east coast. Ridging events have a moistening effect over eastern South Africa and southern Mozambique and are one of the main sources of moisture in summer (Ndarana et al. 2021). Drylines in SAP-E tend to move westward more frequently than drylines in SAP-T or SAP-W. The onset of westward-moving drylines peak at 1200 UTC for SAP-W and 1500 UTC for SAP-E and SAP-T. SAP-E and SAP-T, due to their geographic location, would be influenced by ridging highs more frequently than SAP-W. Low-level cloud associated with ridging high pressure systems often only spreads inland over eastern South Africa during the cooler evening hours, causing westward-moving moisture gradients. Drylines that moved through SAP-E during the late afternoon (1500 UTC) would reach SAP-T later, which could explain the higher frequency of drylines in the morning hours for SAP-T. These SAP-T drylines are often short lived, lasting for 3–6 h.

The preferred location of drylines on the SAP is however over the western interior. Taljaard (1958) first mentioned the tendency of the southern African "moisture front" to form along or just northeast of the usually weak surface trough that develops over the western interior in summer, extending from central Namibia southeastward toward the southern Free State or eastern Northern Cape provinces in South Africa. Howard and Washington (2019) found that drylines over the western interior were often collocated with the 2-m potential temperature maximum and showed that the humidity gradient of the KD was maintained by the Kalahari heat low. Given the nocturnal peak in moisture transport (Spavins-Hicks et al. 2021), the Limpopo LLJ most likely contributes to the regular occurrence of drylines at night on the SAP, SAP-W, and SAP-T (Figs. 9a–c). Despite the peak occurrence of drylines at 1800 and 2100 UTC, onset times of drylines in SAP-W are usually during the hottest time of the day (0900–1200 UTC) with a secondary peak at 1800 UTC. An analysis of eastward-moving drylines showed that this group of drylines shows similar peak onset times as drylines in SAP-W. Dryline movement in SAP-W is almost evenly split between westward and eastward movement, which could explain onset peaks at 0900 UTC, just as for eastward-moving drylines, and 1800 UTC just as for westward-moving drylines. These differences in characteristics suggest that different formation mechanisms are at play for drylines that form over the western interior versus those forming in the east. We suggest that ridging highs in the east and the surface heat trough in the west are most likely responsible for the formation of most drylines across the SAP.

The annual number of dryline days across the SAP does not vary significantly interannually and is not significantly correlated with the Niño-3.4 index. However, much greater variation is observed when the segments are analyzed independently, suggesting greater variation in the location of drylines from year to year. A negative correlation ($r = -0.43$; p value = 0.005) was found between drylines in SAP-W and SAP-E, helping to explain why there is no significant ENSO correlation for SAP as a whole. During years with high dryline occurrence in SAP-W, below-average, or even no (1988/89), drylines were observed in SAP-E, and years with above-average dryline frequencies in SAP-E tended to be the years with below-average dryline frequencies in SAP-W. Of the four high-dryline summers in SAP-E, three coincided with El Niño events (2003/04 was also warm in the Niño-3.4 region, but too weak to be formally classified as El Niño from Fig. 12a) while the four lowest dryline summers coincided with La Niña events. Composite analysis showed that an increased easterly/northeasterly moisture flux over the interior during La Niña events leads to positive specific humidity anomalies over much of the plateau and reduced moisture gradients between the eastern and western segments, and hence fewer drylines on SAP-E. On the other hand, high-dryline summers on SAP-E were associated with southerly anomalies over the Northern Cape province and southern Botswana and drier conditions in the west, hence enhancing surface moisture gradients across SAP-E. There were also distinct differences in the midlevel Botswana high and the amount of uplift in the Angola low region between the high- and low-dryline composites. During high-dryline years, the Botswana high tended to be stronger and the Angola low was weaker. Conversely, during low-dryline years, the Botswana high tended to be weaker and the Angola low was stronger.

Even though the southern African dryline manifests as a surface moisture gradient, variability in midlevel circulation patterns has a large impact on the seasonal frequency of drylines between the western and eastern plateau. Further investigation is necessary to determine the effect of upper-level

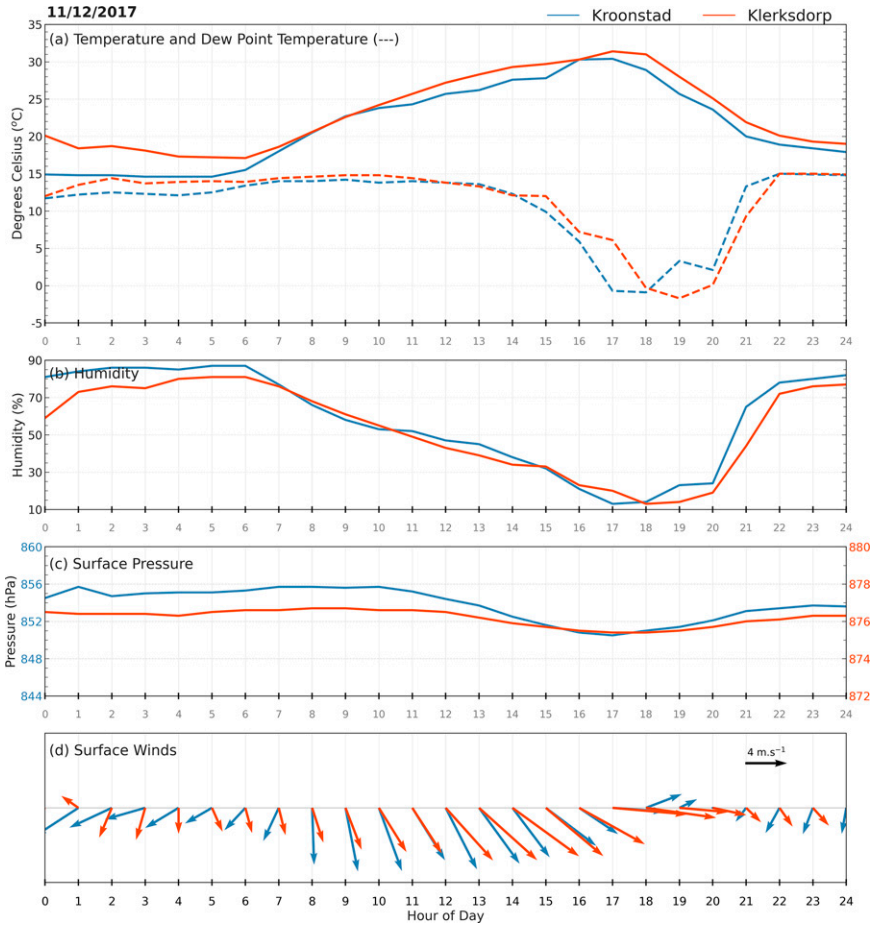

FIG. A1. Hourly observations depicting the dryline passage from the station (see locations in Fig. 2a) at Klerksdorp (blue line) and Kroonstad (orange line) on 11 Dec 2017. The time series are shown for (a) temperature and dewpoint temperature, (b) humidity, (c) surface pressure, and (d) surface winds.

disturbances on drylines in southern Africa and, in turn, the relationship between dryline occurrence and convective development. The work presented in this paper provides a detailed description and helps to improve understanding of drylines in subtropical southern Africa.

Acknowledgments. Author van Schalkwyk thanks South African National Research Foundation (NRF) ACSyS Programme for funding for her Ph.D. Author Blamey acknowledges support of the FLAIR programme, a partnership between the African Academy of Sciences and the Royal Society funded by the U.K. Government's Global Challenges Research Fund. We thank Emma Howard for making her dryline identification algorithm available (https://github.com/emmahoward) and the South African Weather Service for supplying observational data. The authors thank the editor and three anonymous reviewers for their insightful suggestions to improve the paper.

Data availability statement. The ERA5 data (Hersbach. et al. 2018) used were downloaded from the Copernicus Climate Change Service (C3S) Climate Data Store. Satellite imagery was downloaded from EUMETSAT Data Store. Station data in this study are available on request from the South African Weather Service (SAWS) (http://www.weathersa.co.za). Other surface observation data were downloaded from online (www.ogimet.com), as were monthly ERSSTv5 data for the Niño-3.4 region (Huang et al. 2017) (https://climexp.knmi.nl/).

APPENDIX

Dryline Case Study

On the morning of the Vaal Marina tornado, dewpoint values of 15°C (Fig. A1) were reported at Kroonstad and Klerksdorp (see Fig. 2a for locations) in the vicinity of a sharp specific humidity gradient over northeastern South Africa in Fig. 2c. A change in wind direction from northeasterly to northwesterly coincided with a drop in dewpoint during the day. Station observations show that the dryline moved over Kroonstad first, with a sharp decrease in dewpoint

between 1400 and 1700 LST (UTC + 2 h) (Fig. A1). An hour later, the dewpoint had dropped to −1.7°C at Klerksdorp, which represents a drop of 13°C in a matter of 4 h (Fig. A1). Temperatures remained high at these two stations until the early evening hours, but it was cooler east of the dryline (Fig. 2b) where convection had already begun. The dryline was located within a surface trough that had deepened over the previous 24 h. To the west of the surface trough, at 500 hPa, an upper-air trough (not shown) was approaching. A cluster of severe thunderstorms developed over the northern Free State within 75 km east of the dryline (Fig. 2a). One of these storms evolved into a supercell (C. Liesker, meteorologist, 2021, personal communication) and produced the tornado described in section 1. Tornadoes are relatively infrequent events and are mostly observed over the eastern half of South Africa. Between 1948 to 1996 an average of four tornadoes were reported per year (Goliger 1997), but this number has increased since the advent of social media.

REFERENCES

Akter, N., and K. Tsuboki, 2017: Climatology of the premonsoon Indian dryline. *Int. J. Climatol.*, **37**, 3991–3998, https://doi.org/10.1002/joc.4968.

Arnup, S. J., and M. J. Reeder, 2007: The diurnal and seasonal variation of the northern Australian dryline. *Mon. Wea. Rev.*, **135**, 2995–3008, https://doi.org/10.1175/MWR3455.1.

Barimalala, R., F. Desbiolles, R. C. Blamey, and C. Reason, 2018: Madagascar influence on the South Indian Ocean Convergence Zone, the Mozambique Channel Trough and southern African rainfall. *Geophys. Res. Lett.*, **45**, 11 380–11 389, https://doi.org/10.1029/2018GL079964.

——, R. C. Blamey, F. Desbiolles, and C. J. C. Reason, 2020: Variability in the Mozambique Channel Trough and impacts on southeast African rainfall. *J. Climate*, **33**, 749–765, https://doi.org/10.1175/JCLI-D-19-0267.1.

——, ——, ——, and ——, 2021: The influence of southeastern African river valley jets on regional rainfall. *Climate Dyn.*, **57**, 2905–2920, https://doi.org/10.1007/s00382-021-05846-1.

Bechis, H., P. Salio, and J. J. Ruiz, 2020: Drylines in Argentina: Synoptic climatology and processes leading to their genesis. *Mon. Wea. Rev.*, **148**, 111–129, https://doi.org/10.1175/MWR-D-19-0050.1.

Blamey, R. C., and C. J. C. Reason, 2012: Mesoscale convective complexes over southern Africa. *J. Climate*, **25**, 753–766, https://doi.org/10.1175/JCLI-D-10-05013.1.

——, C. Middleton, C. Lennard, and C. J. C. Reason, 2016: A climatology of potential severe convective environments across South Africa. *Climate Dyn.*, **49**, 2161–2178, https://doi.org/10.1007/s00382-016-3434-7.

Cook, C., C. J. C. Reason, and B. C. Hewitson, 2004: Wet and dry spells within particularly wet and dry summers in the South African summer rainfall region. *Climate Res.*, **26**, 17–31, https://doi.org/10.3354/cr026017.

De Coning, E., 2011: Two tornadoes and snow occurred on one day in South Africa. EUMETSAT, https://www.eumetsat.int/two-tornadoes-and-snow-south-africa.

——, and B. F. Adam, 2000: The tornadic thunderstorm events during the 1998-1999 South African summer. *Water SA*, **26**, 361–376, https://wrcwebsite.azurewebsites.net/wp-content/uploads/mdocs/WaterSA_2000_03_1263.pdf.

——, ——, and L. Banitz, 2000: A severe weather event on 29 December 1997: Synoptic and mesoscale perspectives. *Water SA*, **26**, 137–146, https://wrcwebsite.azurewebsites.net/wp-content/uploads/mdocs/WaterSA_2000_02_1252.pdf.

Driver, P., and C. J. C. Reason, 2017: Variability in the Botswana High and its relationships with rainfall and temperature characteristics over southern Africa. *Int. J. Climatol.*, **37**, 570–581, https://doi.org/10.1002/joc.5022.

Duell, R. S., and M. S. Van Den Broeke, 2016: Climatology, synoptic conditions, and misanalyses of Mississippi River valley drylines. *Mon. Wea. Rev.*, **144**, 927–943, https://doi.org/10.1175/MWR-D-15-0108.1.

Dyson, L. L., 2015: A heavy rainfall sounding climatology over Gauteng, South Africa, using self-organising maps. *Climate Dyn.*, **45**, 3051–3065, https://doi.org/10.1007/s00382-015-2523-3.

——, N. Pienaar, A. Smit, and A. Kijko, 2021: An ERA-Interim HAILCAST hail climatology for southern Africa. *Int. J. Climatol.*, **41**, 262–277, https://doi.org/10.1002/joc.6619.

Engelbrecht, C. J., W. A. Landman, F. A. Engelbrecht, and J. Malherbe, 2015: A synoptic decomposition of rainfall over the Cape south coast of South Africa. *Climate Dyn.*, **44**, 2589–2607, https://doi.org/10.1007/s00382-014-2230-5.

Gijben, M., 2012: The lightning climatology of South Africa. *S. Afr. J. Sci.*, **108**, 740, https://doi.org/10.4102/sajs.v108i3/4.740.

Goliger, A. M., R. V. Milford, B. F. Adam, and M. Edwards, Eds., 1997: *Inkanyamba Tornadoes in South Africa.* CSIR and Weather Bureau, 77 pp.

Hart, N. C. G., C. J. C. Reason, and N. Fauchereau, 2010: Tropical–extratropical interactions over southern Africa: Three cases of heavy summer season rainfall. *Mon. Wea. Rev.*, **138**, 2608–2623, https://doi.org/10.1175/2010MWR3070.1.

——, ——, and ——, 2013: Cloud bands over southern Africa: seasonality, contribution to rainfall variability and modulation by the MJO. *Climate Dyn.*, **41**, 1199–1212, https://doi.org/10.1007/s00382-012-1589-4.

Hersbach, H., and Coauthors, 2018: ERA5 hourly data on single levels from 1979 to present. Copernicus Climate Change Service (C3S) Climate Data Store (CDS), accessed 2020, https://doi.org/10.24381/cds.adbb2d47.

Hoch, J., and P. Markowski, 2005: A climatology of springtime dryline position in the U.S. Great Plains region. *J. Climate*, **18**, 2132–2137, https://doi.org/10.1175/JCLI3392.1.

Howard, E., and R. Washington, 2019: Drylines in southern Africa: Rediscovering the Congo air boundary. *J. Climate*, **32**, 8223–8242, https://doi.org/10.1175/JCLI-D-19-0437.1.

——, ——, and K. I. Hodges, 2019: Tropical lows in southern Africa: Tracks, rainfall contributions, and the role of ENSO. *J. Geophys. Res. Atmos.*, **124**, 11 009–11 032, https://doi.org/10.1029/2019JD030803.

Huang, B., and Coauthors, 2017: Extended Reconstructed Sea Surface Temperature, version 5 (ERSSTv5): Upgrades, validations, and intercomparisons. *J. Climate*, **30**, 8179–8205, https://doi.org/10.1175/JCLI-D-16-0836.1.

Lekoloane, L. E., M.-J. M. Bopape, T. G. Rambuwani, T. Ndarana, S. Landman, P. Mofokeng, M. Gijben, and N. Mohale, 2021: A dynamic and thermodynamic analysis of the 11 December 2017 tornadic supercell in the Highveld of South Africa. *Wea. Climate Dyn.*, **2**, 373–393, https://doi.org/10.5194/wcd-2-373-2021.

Malherbe, J., F. A. Engelbrecht, W. A. Landman, and C. J. Engelbrecht, 2012: Tropical systems from the southwest Indian Ocean making landfall over the Limpopo River

Basin, southern Africa: A historical perspective. *Int. J. Climatol.*, **32**, 1018–1032, https://doi.org/10.1002/joc.2320.

Marengo, J. A., W. R. Soares, C. Saulo, and M. Nicolini, 2004: Climatology of the low-level jet east of the Andes as derived from the NCEP–NCAR reanalyses: Characteristics and temporal variability. *J. Climate*, **17**, 2261–2280, https://doi.org/10.1175/1520-0442(2004)017<2261:COTLJE>2.0.CO;2.

Morake, D. M., R. C. Blamey, and C. J. C. Reason, 2021: Long-lived mesoscale convective systems over eastern South Africa. *J. Climate*, **34**, 6421–6439, https://doi.org/10.1175/JCLI-D-20-0851.1.

Mulenga, H. M., M. Rouault, and C. J. C. Reason, 2003: Dry summers over northeastern South Africa and associated circulation anomalies. *Climate Res.*, **25**, 29–41, https://doi.org/10.3354/cr025029.

Munday, C., and R. Washington, 2017: Circulation controls on southern African precipitation in coupled models: The role of the Angola low. *J. Geophys. Res. Atmos.*, **122**, 861–877, https://doi.org/10.1002/2016JD025736.

Ndarana, T., S. Mpati, M. J. Bopape, F. Engelbrecht, and H. Chikoore, 2021: The flow and moisture fluxes associated with ridging South Atlantic Ocean anticyclones during the subtropical southern African summer. *Int. J. Climatol.*, **41**, E1000–E1017, https://doi.org/10.1002/joc.6745.

Parker, W. S., 2016: Reanalyses and observations: What's the difference? *Bull. Amer. Meteor. Soc.*, **97**, 1565–1572, https://doi.org/10.1175/BAMS-D-14-00226.1.

Pielke, R. A., and M. Segal, 1986. Mesoscale circulations forced by differential terrain heating. *Mesoscale Meteorology and Forecasting.* 1st ed. P. S. Ray, Ed., Amer. Meteor. Soc., 516–548.

Qin, R., and M. Chen, 2017: Impact of a front–dryline merger on convection initiation near a mountain ridge in Beijing. *Mon. Wea. Rev.*, **145**, 2611–2633, https://doi.org/10.1175/MWR-D-16-0369.1.

Rae, K. J., 2014. A modified supercell composite parameter for supercell thunderstorms over the Gauteng Province, South Africa. M.S. thesis, Dept. of Geography, Geoinformatics and Meteorology, University of Pretoria, 182 pp.

Rapolaki, R. S., R. C. Blamey, J. C. Hermes, and C. J. C. Reason, 2019: A classification of synoptic weather patterns linked to extreme rainfall over the Limpopo River Basin in southern Africa. *Climate Dyn.*, **53**, 2265–2279, https://doi.org/10.1007/s00382-019-04829-7.

Reason, C. J. C., 2016: The Bolivian, Botswana, and Bilybara highs and Southern Hemisphere drought/floods. *Geophys. Res. Lett.*, **43**, 1280–1286, https://doi.org/10.1002/2015GL067228.

——, and D. Jagadheesha, 2005: A model investigation of recent ENSO impacts over southern Africa. *Meteor. Atmos. Phys.*, **89**, 181–205, https://doi.org/10.1007/s00703-005-0128-9.

——, R. J. Allan, J. A. Lindesay, and T. J. Ansell, 2000: ENSO and climatic signals across the Indian Ocean Basin in the global context: Part I, Interannual composite patterns. *Int. J. Climatol.*, **20**, 1285–1327, https://doi.org/10.1002/1097-0088(200009)20:11<1285::AID-JOC536>3.0.CO;2-R.

——, W. Landman, and W. Tennant, 2006: Seasonal to decadal prediction of southern African climate and its links with variability of the Atlantic Ocean. *Bull. Amer. Meteor. Soc.*, **87**, 941–956, https://doi.org/10.1175/BAMS-87-7-941.

Rhea, J. O., 1966: A study of thunderstorm formation along drylines. *J. Appl. Meteor. Climatol.*, **5**, 263–285, https://doi.org/10.1175/1520-0450(1966)005<0058:ASOTFA>2.0.CO;2.

Schaefer, J. T., 1974: The life cycle of the dryline. *J. Appl. Meteor.*, **13**, 444–449, https://doi.org/10.1175/1520-0450(1974)013<0444:TLCOTD>2.0.CO;2.

——, 1986: The dryline. *Mesoscale Meteorology and Forecastingz*, 1st ed. P. S. Ray, Ed., Amer. Meteor. Soc., 549–572.

Schultz, D. M., C. C. Weiss, and P. M. Hoffman, 2007: The synoptic regulation of dryline intensity. *Mon. Wea. Rev.*, **135**, 1699–1709, https://doi.org/10.1175/MWR3376.1.

Spänkuch, D., J. Güldner, H. Steinhagen, and M. Bender, 2011: Analysis of a dryline-like feature in northern Germany detected by ground-based microwave profiling. *Meteor. Z.*, **20**, 409–421, https://doi.org/10.1127/0941-2948/2011/0222.

Spavins-Hicks, Z. D., R. Washington, and C. Munday, 2021: The Limpopo low-level jet: Mean climatology and role in water vapor transport. *J. Geophys. Res. Atmos.*, **126**, e2020JD034364, https://doi.org/10.1029/2020JD034364.

Stull, R. B., 2017. Water vapor. *Practical Meteorology: An Algebra-Based Survey of Atmospheric Science*, Sundog Publishing, 87–118.

Taljaard, J. J., 1958. South African air-masses: Their properties, movement and associated weather. Ph.D. thesis, University of Witwatersrand, 221 pp.

——, 1972: Synoptic meteorology of the Southern Hemisphere. *Meteorology of the Southern Hemisphere, Meteor. Monogr.*, No. 35, Amer. Meteor. Soc., 139–211.

——, 1986: Change of rainfall distribution and circulation patterns over southern Africa in summer. *J. Climatol.*, **6**, 579–592, https://doi.org/10.1002/joc.3370060602.

——, 1996: Atmospheric circulation systems, synoptic climatology and weather phenomena of South Africa. South African Weather Bureau Tech. Rep. 32, 98 pp.

Thema, E., 2013: Severe thunderstorms with golf ball size hail and flash floods hit Gauteng province of South Africa in late November. EUMETSAT, https://www.eumetsat.int/massive-hailstorm-over-gauteng-south-africa.

Thoithi, W., R. C. Blamey, and C. J. C. Reason, 2021: Dry spells, wet days, and their trends across southern Africa during the summer rainy season. *Geophys. Res. Lett.*, **48**, e2020GL091041, https://doi.org/10.1029/2020GL091041.

Tyson, P. D., and R. A. Preston-Whyte, 2000: *The Weather and Climate of Southern Africa.* Oxford University Press, 396 pp.

Webster, E. M., 2019: A synoptic climatology of continental tropical low pressure systems over southern Africa and their contribution to rainfall over South Africa. M.S. thesis, Department of Geography Geoinformatics and Meteorology, University of Pretoria, 96 pp.

Weldon, D., and C. J. C. Reason, 2014: Variability of rainfall characteristics over the South Coast region of South Africa. *Theor. Appl. Climatol.*, **115**, 177–185, https://doi.org/10.1007/s00704-013-0882-4.

Weston, K. J., 1972: The dry-line of northern India and its role in cumulonimbus convection. *Quart. J. Roy. Meteor. Soc.*, **98**, 519–531, https://doi.org/10.1002/qj.49709841704.